Studies for the Loss of Atomic and Molecular Species from Io

William H. Smyth

Atmospheric and Environmental Research, Inc.
840 Memorial Drive
Cambridge, MA 02139-3794

Report for the Periods of
March 23 to May 22, 1997

I. Introduction

The general objective of this project is to advance our theoretical understanding of Io's atmosphere by studying how various atomic and molecular species are lost from this atmosphere and are distributed near the satellite and in the circumplanetary environment of Jupiter. The project is divided into well-defined studies described for the likely dominant atmospheric gases involving species of the SO_2 family (SO_2, SO, O_2, O, S) and for the trace atmospheric gas atomic sodium. The relative abundance of the members of the SO_2 family and Na (and its parent NaX) at the satellite exobase and their relative spatial densities beyond in the extended corona of Io are not well known but will depend upon a number of factors including the upward transport rate of gases from below, the velocity distribution and corresponding escape rate of gases at the exobase, and the operative magnetospheric/solar-photon driven chemistry for the different gases. This question of relative abundance will be studied in this project.

In order to address this question, we will undertake theoretical modeling studies for the distribution and time variability of these exospheric gases in Io's corona/extended clouds and thereby evaluate the importance of various physical processes that shape their relative abundances and escape rates. Our primary objective will be to study near-Io emission observations for O, S, and Na, most of which have already been acquired and some of which are scheduled to be acquired in 1996-1997 as part of the larger coordinated International Jupiter Watch Observational Campaign to support the Galileo mission. A secondary objective will be to continue the study of various larger-spatial-scale groundbased sodium and spacecraft (Voyager and Galileo) SO_2^+ observations in order to address related issues and to lay the groundwork for larger-spatial-scale O and S observations likely to be obtained in the near future. The proposed studies are of scientific importance in understanding (1) the atmosphere of the satellite, (2) the interactions of the magnetospheric plasma and the atmosphere, (3) the nature and composition of the heavy ion sources for the plasma torus, (4) the impact of these gases on the larger magnetosphere, and (5) the spatial distribution of these gases in the magnetosphere and beyond in the larger solar wind environment.

Near-Io observations for this project will be made available in four collaborative efforts established with

(1) F. Scherb of the University of Wisconsin-Madison who from groundbased facilities in 1990-1996 very successfully obtained synoptic observations of [O I] 6300 Å emission near Io and in 1996-1998 will continue these synoptic observations, search for [O I] 5577

Å emission, and add a new Fabry-Perot program element using the new WIYN telescope at Kitt Peak to obtain very-high spatial resolution images near Io in the [O I] 6300 Å and Na 5890 Å emission lines,

(2) G. E. Ballester of the University of Michigan who with HST has acquired cycle IV and will be acquiring cycle V observations for O and S near Io in various UV emission lines,

(3) L. M. Trafton of the University of Texas who has obtained in 1984-1989, and in his ongoing program in 1995 and 1996, groundbased observations for the north-south spatial distribution and spectral line shape of sodium (5890 Å, 5896 Å) emissions near Io, and

(4) N. M. Schneider of the University of Colorado-Boulder who obtained in 1987 from groundbased facilities an extensive set of observations for the east-west spatial distribution and spectral line shape of sodium emissions near Io, which exactly overlap the October 1987 observations of Trafton.

These near-Io emissions exhibit time variability with Io System III longitude and Io east-west location. The general three year plan of research for these studies is outlined in Table 1.

II. Summary of Work Performed in the Fourth Bi-Month Periods

Work accomplished in fourth bi-monthly period includes (1) the completion of an initial study for the SO_2 source rate at Io exobase based on presently available Galileo spacecraft data and (2) the completion of a study for the total neutral energy loss rate of atomic oxygen and sulfur from Io and the implications for local magnetospheric interactions. This research is summarized briefly below and is the subject of two papers that are nearing completion and are to be submitted for publication in the fifth bi-monthly period. In addition, earlier research work included in a paper entitled" Io's Sodium Corona and Spatially Extended Cloud: A Consistent Flux Speed Distribution" (Smyth and Combi 1997) appeared in the March 1997 issue of Icarus. A copy of this paper is attached to this report.

To estimate the source strength of SO_2 at the Io's exobase, we have used information for the spatial distribution of SO_2^+ obtained from the Galileo spacecraft in its December 7, 1995 encounter with Io when it flew downstream of the satellite through Io's magnetospheric wake with a closest approach distance above the surface of ~900 km. An SO_2^+ density profile was deduced from magnetic field fluctuations with periods of ~2 to 3 sec measured by the Galileo

magnetometer and interpreted as ion cyclotron waves produced by fresh SO_2^+ Iogenic pickup ions created near Io. Calculations for the SO_2^+ density profile along the Galileo trajectory were undertaken using the AER neutral cloud model for SO_2, where SO_2^+ is produced from SO_2 by electron impact and charge exchange reactions in the plasma torus. By adopting for SO_2 the isotropic incomplete collisional cascade flux source velocity distribution recently deduced for atomic sodium at the exobase (Smyth and Combi 1997), we were able to match the minimum SO_2^+ density profile determined by Huddleston et al. (1997) in their analysis of the ion cyclotron waves and the SO_2^+ model calculated density profile for an SO_2 source rate at Io's exobase of ~4 x 10^{27} molecules sec^{-1} (225 kg sec^{-1}) which created in the magnetosphere a total SO_2^+ production rate of 1.1 x 10^{26} ions sec^{-1} (29 kg sec^{-1}). Most (>90%) of the SO_2 that undergoes interactions in the plasma torus is, however, rapidly dissociated primarily by electron impact producing O, S, SO, and O_2 which subsequently undergo ionization and charge exchange reactions in the plasma torus producing additional mass and energy pickup plasma loading rates that are larger than the SO_2^+ production rate of 29 kg sec^{-1} by more than an order of magnitude. This substantial exobase source rate for SO_2 of ~4 x 10^{27} molecules sec^{-1} is a factor of only about two less than the estimated SO_2 source rate of 8.9 x 10^{27} s^{-1} suggested from the earlier analysis of the O(^{1}D) 6300 Å emission brightness near Io by Scherb and Smyth (1993). About half of the molecules in the incomplete collisional cascade source distribution for SO_2 are not energetic enough to escape the Lagrange sphere of the satellite (~10,550 km or 5.81 R_{Io}) and hence will populate ballistic orbits above the exobase and create a density gradient in the satellite corona. This density gradient plays a central role in matching the steepness of the deduced SO_2^+ density profile at closer distances to Io (within a radius of ~3 satellite radii). The agreement of the model and observationally derived SO_2^+ density profiles thus implies that sodium and SO_2 have a very similar incomplete collisional cascade flux velocity distribution at the satellite exobase as would be expected if sodium atoms (a trace species in the atmosphere) were produced in the same volume by the same incomplete collisional cascade processes. This agreement also implies that the collisional cascade flux velocity distribution at the exobase for other species, such as atomic oxygen and atomic sulfur, would also be similar.

Estimates for the rate at which energy is lost by O and S atoms escaping from near Io's exobase because of the interaction of Io's atmosphere with the corotating magnetospheric plasma have been made for three source processes: (1) incomplete collisional cascade (2) slow-velocity charge exchange and direct ejection, and (3) fast-velocity charge exchange. For the incomplete collisional cascade, the energy loss rate is estimated to be 7.5 x 10^9 watts. If this energy loss rate is as expected ~20% of the total incomplete collisional cascade energy deposition rate in the heating layer, then it implies that 56% of the upstream ion kinetic energy flow rate of 6.7 x 10^{10}

watts for a reference cross sectional area of an Io disk area is required for this process. This is a factor of 2.8 times larger than the previously adopted value of 20% and implies that the effective deflection of magnetospheric plasma out of the interaction region near Io is less than previously thought for the collisional cascade process. For slow-velocity charge exchange and direct ejection (centered about 20 km/sec), the energy loss rate is estimated to be 3.3×10^{10} watts, which is 50% of the reference upstream ion kinetic energy flow rate. For fast-velocity charge exchange (centered about ~60 km/sec), the energy loss rate is much larger and is the dominant energy loss mechanism with an estimated value of 6.04×10^{11} watts, which is ~900% of the reference upstream ion kinetic energy flow rate. The total estimated neutral energy loss rate for all three processes (including radiative loss processes) is 6.75×10^{11} watts and is too large by an order of magnitude to be provided by the reference upstream initial ion kinetic energy flow rate. The required neutral energy loss rate (i.e., power) is, however, matched by the magnetic field energy density flow rate of 7.9×10^{11} watts for the upstream reference area and implies that the charge exchange energy loss rates are capable of producing a large pickup current as well as a significant reduction in the local planetary magnetic field in the interaction region near Io. The magnitude of the current and the reduction in the local magnetic field will depend critically upon the volume of the interaction region established by the solution of the three-dimensional magnetospheric flow problem past Io including these complex plasma-neutral interactions. Rough estimates suggest a pickup current in the range of $\sim 4 \times 10^6$ to 2×10^7 A and a reduction (ΔB) in the local magnetic planetary field of ~450 nT. This estimated reduction of the magnetic field is similar to the remaining and unexplained ΔB of ~400-500 nT determined in a recent analysis (Khurana et al. 1997) of the magnetic field depression measured near Io by the Galileo Magnetometer (Kivelson et al. 1996 a,b) and attributed by them to an internal magnetic dipole field for Io. Hence, we conclude that the reduction of the planetary magnetic field measured by Galileo near Io may be a direct reflection of the local charge exchange source and need not require an internal magnetic field for the satellite.

REFERENCES

Huddleston, D.E., R.J. Strangeway, J. Warnecke, C.T. Russell, and M.G. Kivelson, Ion Cyclotron Waves Observed at Galileo's Io Encounter: Warm Plasma Dispersion Analysis. Geophys. Res. Letts., in press (preprint), 1997.

Khurana, K. K., Kivelson M. G., and Russell, C. T. (1997) Does Io have an Internal Magnetic Field?, Presented at the Magnetospheres of the Outer Planets Conference, March 17-21, 1997, Boulder, Colorado.

Kivelson M. G., Khurana, K. K., Walker, R. J., Russell, C. T., Linker, J. A., Southwood, D. J., and Polanskey, C. (1996a) A Magnetic Signature at Io: Initial Report from the Galileo Magnetometer, Science 273, 337-340.

Kivelson, M. G., Khurana, K. K., Walker, R. J., Warnecke, J., Russell, C. T., Linker, J. A., Southwood, D. J., and Polanskey, C. (1996b) Io's Interaction with the Plasma Torus: Galileo Magnetometer Report Science 274, 396-398.

Scherb, F. and W.H. Smyth, Variability of [O I] 6300-Å Emission Near Io. J. Geophys. Res. 98, 18729-18736, 1993.

Smyth, W. H. and M. R. Combi, Io's Sodium Exosphere and Spatially Extended Cloud: A Consistent Flux Speed Distribution. Icarus 126, 58-77, 1997.

Table 1

Three Year Plan of Research for Studies for the Loss of Atomic and Molecular Species from Io

Subject	Year 1	Year 2	Year 3
Studies for the SO_2 Family	Analyze HST (cycle IV) UV data for O and S and available [O I] 6300 Å synoptic data for O using the O, S, SO and SO_2 cloud models; improve model execution time, update chemistry and refine the model description of the plasma torus.	Analyze the HST (cycle V) UV data for O and S; initiate analysis of Fabry-Perot image data for [O I] 6300 Å and [O I] 5577 Å (if relevant); re-analyze Voyager SO_2^+ data; determine sources rates and constraints on O, S, SO and SO_2 for the individual studies.	Complete analysis of UV and optical data; undertake the comparative and collective assessment of the individual studies for O, S, Na and SO_2^+ to probe the nature of the atomic and molecular species in Io's atmosphere and their implications for the Jupiter system.
Studies for Sodium	Continue the analysis of the 1987 east-west emission data set; initiate analysis of the same-date 1987 north-south emission data; refine model description of the plasma torus; re-evaluate the Na source at Io for the directional feature.	Complete analysis of the 1987 east-west emission data set; undertake analysis of other select years of the north-south emission data set; determine the nature and variability of the Na source conditions and their dependence on east-west and System III effects; analyze Fabry-Perot images for sodium and compare with [O I] 6300 Å images; assess the importance of the electron impact excitation and/or nonuniform gas distributions as a cause for asymmetric brightness distributions about Io.	

ICARUS 126, 58–77 (1997)
ARTICLE NO. IS965633

Io's Sodium Corona and Spatially Extended Cloud: A Consistent Flux Speed Distribution

WILLIAM H. SMYTH

Atmospheric and Environmental Research, Inc., Cambridge, Massachusetts 02139
E-mail: smyth@aer.com

AND

MICHAEL R. COMBI

Space Physics Research Laboratory, University of Michigan, Ann Arbor, Michigan 48109

Received November 1, 1993; revised October 3, 1996

A data set composed of different groundbased observations for Io's sodium corona and spatially extended sodium cloud and covering the spatial range from Io's nominal exobase of 1.4 satellite radii to east–west distances from Io of ±100 satellite radii (R_{Io}) is used to investigate the velocity distribution of sodium at the exobase. The data set is composed of the novel 1985 eclipse measurements of Schneider *et al.* (1991, *Astrophys. J.* 368, 298–315) acquired from ~1.4 to ~10 R_{Io}, the 1985 east–west emission data of Schneider *et al.* acquired from ~4 to ~40 R_{Io}, and sodium cloud image data acquired near Io's orbital plane from ~10 to ~100 R_{Io} by a number of different observers in the 1976 to 1983 time frame. A one-dimensional east–west profile that contains Io is constructed from the data set and is analyzed using the sodium cloud model of Smyth and Combi (1988, *Astrophys. J. Supp.* 66, 397–411; 1988, *Astrophys. J.* 328, 888–918). When the directional feature in the trailing cloud is either north or south of this east–west line (i.e., not at the null condition), an isotropic modified [incomplete ($\alpha = 7/3$) collisional cascade] sputtering flux speed distribution at the satellite exobase with a peak at 0.5 km sec^{-1} provides an excellent fit to the data set for a sodium source of 1.7×10^{26} atoms sec^{-1}. In particular, the model calculation reproduces (1) the essentially symmetric column density distributions exhibited by the eclipse measurements about Io within the Lagrange sphere radius (5.85 R_{Io}, i.e., the gravitational grasp of the satellite), (2) the change in the slope of the column density observed just beyond the Lagrange sphere radius in the east–west profile of the forward cloud, but not in the trailing cloud, and (3) the distinctly different east–west brightness profiles exhibited by the forward and trailing clouds in the emission data at the more distant (~ ±20–100 R_{Io}) portions of the cloud. In contrast, the speed dispersion at the exobase for either an isotropic Maxwell–Boltzmann flux speed distribution or an isotropic classical ($\alpha = 3$) sputtering flux speed distribution (which has a higher velocity-tail population than the Maxwell–Boltzmann, but not as high as the incomplete collisional cascade sputtering distribution) is shown to be inadequate to fit the data set. To fit the enhanced trailing east–west profile observed when the directional feature is at the null condition, an additional enhanced high-speed (~15–20 km sec^{-1}) sodium population is required which is nonisotropically ejected from the satellite exobase so as to preferentially populate the trailing cloud. The need for such a nonisotropic high-speed population of sodium has also been recognized in the earlier modeling analysis of the directional features (Pilcher *et al.*, 1984, *Astrophys. J.* 287, 427–444), in the more recent lower-velocity component required in modeling the sodium zenocorona (Smyth and Combi, 1991, *J. Geophys. Res.* 96, 22711–22727; Flynn *et al.*, 1992, *Icarus* 99, 115–130), and in the very recent modeling of the directional feature reported by Wilson and Schneider (1995, *Bull. Am. Astron. Soc.* 27, 1154). A complete sodium source rate speed distribution function at Io's exobase from 0–100 km sec^{-1} is then constructed by combining the isotropic modified [incomplete ($\alpha = 7/3$) collisional cascade] sputtering flux speed distribution, the nonisotropic directional feature (lower-velocity zenocorona) source (~15–20 km sec^{-1}), and the higher-speed (~20–100 km sec^{-1}) charge-exchange source required to simulate the sodium zenocorona far from Jupiter.

1. INTRODUCTION

Atomic sodium in the Jupiter system originating from a satellite source at Io has been observed in the D_2 (5889.95 Å) and D_1 (5895.92 Å) emission lines during the past 25 yr from groundbased facilities. Using an observing slit, the sodium emission which is excited by solar resonance scattering was first discovered in 1972 by Brown (1974) very near Io, where its intensity is brightest [~many tens of kiloRaleighs (kR)] and where the sodium density is dominated by low-speed (~2 km sec^{-1} or less) ballistic atom orbits in the satellite "corona." By occultation of the

0019-1035/97 $25.00

bright region near Io, image observations (Murcray 1978; Murcray and Goody 1978; Matson *et al.* 1978) were first acquired in 1976 and 1977 for fainter (~ few to ~0.5 kR) sodium more distant from Io but still near its circular orbit (radius of 5.9 Jupiter radii) about the planet and revealed the presence of a predominant "forward cloud" and a less spatially extensive "trailing cloud" that moved with the satellite. This sodium has been characterized primarily by a source of low-speed (~2.6–4 km sec^{-1}) atoms that have sufficient energy to just escape from Io with an excess velocity of only ~1 km sec^{-1} (or so) and thereby remain gravitationally bound to Jupiter fairly near the satellite orbit. Additional observations (Pilcher *et al.* 1984; Goldberg *et al.* 1984) of even fainter (~1 to 0.2 kR) sodium in the early 1980's revealed a "directional feature" attached to Io in the trailing cloud that oscillated north and south about the satellite plane with a phase and period determined by the Io System III longitude angle. This sodium source was characterized by atoms with speeds ~20 km sec^{-1} ejected nonisotropically from the satellite so as to populate the trailing cloud and the circumplanetary space at larger radial distances beyond Io's orbit. From earlier slit measurements in 1974 (Trafton and Macy 1978), fainter (~30 R) sodium emissions well beyond Io's orbit had been observed at a radial distance of ~60 planetary radii, while from more recent images (Mendillo *et al.* 1990), very faint (~1 R) sodium emissions were observed at radial distances of ~400–500 planetary radii. Sodium at these larger radial distances is called the "magneto-nebula" or "sodium zenocorona" and is thought to be populated primarily by a nonisotropic charge-exchange source of high speed (~15–100 km sec^{-1}) atoms at Io with velocity skewed in the forward direction of corotational plasma motion past the satellite, and secondarily by a narrow forward sodium jet produced by a spatially distributed molecular ion source (Wilson and Schneider 1994). Most of this sodium escapes the Jupiter system, forms a sodium pause in the sunward direction at ~2300 planetary radii because of solar radiation acceleration, and is eventually lost to the solar wind by photoionization (Smyth and Combi 1991).

The observations of sodium emissions on many different spatial scales in the Jupiter system thus indicate that its atomic source at Io's exobase must have a wide dispersion of speeds. Modeling of these observations has in the past been mostly undertaken separately for only one of these spatial regions at a time. Although the higher velocity dispersions for the sodium zenocorona may be reasonably well understood because of its large spatial structure and the lack of any significant sodium lifetime impact of the magnetosphere, a consistent source for the slower sodium in Io's corona and in the forward and trailing clouds near its orbit has not been established. The recent determination of the sodium spatial profile in the Io corona obtained from the groundbased eclipse data of Schneider (1988; Schneider *et al.* 1987, 1991) coupled with earlier emission observations, however, now provides a viable observational base from which it is possible to pursue the nature of this slower sodium. The investigation of a consistent exobase sodium source for Io's corona and the forward and trailing clouds near its orbit is therefore undertaken in this paper. A consistent flux speed distribution at the exobase is determined, and the corresponding sky-plane spatial distribution of sodium near Io is presented. Sodium source information obtained from previous modeling analysis of Io's corona and the forward and trailing clouds is first summarized in Section 2. The observational data base to be investigated in this paper is presented in Section 3. Modeling of an east–west spatial profile determined from this observational data base is undertaken in Section 4. Discussion and conclusions are presented in Section 5.

2. EARLIER SODIUM MODELING

The major modeling analysis studies for the spatial distribution of sodium near Io and its orbit are summarized in Table I. The summary is divided into three observed spatial regions: (1) the Io corona located within the satellite Lagrange sphere (average radius of 5.81 R_{Io} or ~3 arcsec), (2) the neutral cloud located beyond the Lagrange sphere and near Io's orbit, and (3) the north–south oscillating directional feature, observed to trail Io in its orbit. Modeling analysis studies for the Io corona are further subdivided into early observations of the average intensity in an 8 × 3 arcsec slit centered on Io reported by Bergstralh *et al.* (1975, 1977) that indicated an east–west intensity asymmetry of ~1.25 and later observations for one-dimensional column density profiles within the Lagrange sphere reported by Schneider *et al.* (1987, 1991).

2.1. Corona: East–West Intensity Asymmetry

In Table I, the early studies of Smyth (1983) for sodium atoms ejected monoenergetically from Io's exobase established that small scale structures in the D-line intensity profile observed as a function of the Io geocentric phase angle (Bergstralh *et al.* 1975, 1977) could arise from modulation of the atoms' escape rate from Io caused by the action of solar radiation acceleration in the D-lines. These modulations occur primarily for exobase speeds near 2.0 and 2.1 km sec^{-1}, which are near the escape-speed threshold of the Lagrange sphere. Later studies of Smyth and Combi (1987a) showed that the main reason for the east–west intensity asymmetry was, however, an east–west electric field which altered the plasma properties at Io's orbit so as to increase the sodium lifetime and hence sodium abundance when Io was preferentially east of Jupiter. More complex modeling studies of Smyth and Combi (1988b) constrained the flux velocity dispersion for sodium at Io's exobase by simultaneously fitting the average east–west

TABLE I
Summary of Modeling Studies for the Spatial Distribution of Sodium Near Io and Its Orbit

		Sodium Source								Sodium Lifetime		Orbital Dynamics			
		Mono-energetic Atom Ejection	Maxwell-Boltzman Flux Distribution		Cascade Flux Speed Distribution										
Spatial Region	Topic Studied	Speed (km s^{-1})	T (K)	v_{peak} (km s^{-1})	α	v_b (km s^{-1})	v_{peak} (km s^{-1})	v_{max} (km s^{-1})	Angular Nature[a]	Plasma Torus Description	Lifetime (hrs)	Io's Mass Included	Jupiter's Mass Included	Radiation Pressure Included	Reference
I. Corona	e-w intensity asymmetry[b]	2.0-2.6	-	-	-	-	-	-	isotropic	cut-off	20	yes	yes	yes	Smyth 1983
	e-w intensity asymmetry[b]	2.6	-	-	-	-	-	-	isotropic	2-D	variable	yes	yes	yes	Smyth and Combi 1987a
	e-w intensity asymmetry[b]	-	460; 12,300	0.71; 3.65	7/3	<0.4; 2.2	<0.5; 2.9	46.6	band, isotropic	2-D	variable	yes	yes	yes	Smyth and Combi 1988b
	column-density profile[c]	2.6	-	-	-	-	-	-	isotropic	2-D	varialbe	yes	yes	yes	Smyth and Combi 1987b,c
	column-density profile[c]	-	-	-	3	0[d]	-	∞	isotropic	cut-off	3, ∞	yes	no	no	McGrath 1988
	column-density profile[c]	-	1000	1.04	-	-	-	-	isotropic	uniform	∞	yes	no	no	Summers et al. 1989
	column-density profile[c]	3.0	-	-	-	-	-	-	isotropic	uniform	?	yes	no	no	Ip 1990
	column-density profile[e]	-	1500	1.28	-	-	-	-	isotropic	uniform	∞	yes	no	no	Schneider et al. 1991
II. Cloud	general spatial nature	3.5	-	-	-	-	-	-	isotropic	uniform	30, 47	yes	yes	no	Carlson et al. 1975
	general spatial nature	-	5000	2.3	-	-	-	-	isotropic	long-lived limit	-	no	yes	no	Fang et al. 1976
	evolution and 2-D nature	2, 3	-	-	-		-	-	isotropic	cut-off	50	yes	yes	no	Smyth and McElroy 1977
	1-D brightness morphology[f]	-	-	-	3	4	4	∞	I-L hemisphere[g]	uniform	28	yes	yes	no	Matson et al. 1978
	2-D brightness morphology[h]	2.6, 3	-	-	-	-	-	-	I, I-T hemisphere[i]	cut-off	15, 20	yes	yes	no	Smyth and McElroy 1978
	e-w orbital asymmetry[j]	2.6	-	-	-	-	-	-	I-T hemisphere[i]	cut-off	20	yes	yes	yes	Smyth 1979
	radial and vertical structure	(3,5,7,9,11,13)[k]	-	-	-	-	-	-	I hemisphere	uniform	56	no	yes	no	Macy and Trafton 1980
	1-D brightness morphology	-	-	-	3[l]	4[l]	4[l]	∞[l]	I-L hemisphere[l]	1-D	variable	yes	yes	no	Goldberg et al. 1980
	e-w orbital asymmetry	2.6	-	-	-	-	-	-	I hemisphere	cut-off	20	yes	yes	yes	Smyth 1983
	2-D brightness morphology	2.6	-	-	-	-	-	-	band, isotropic	2-D	variable	yes	yes	yes	Smyth and Combi 1988b
III. Directional Feature	spacetime structure[m]	~20	-	-	-	-	-	-	O, ~⊥ to Io's motion	2-D	variable	yes	yes	yes	Pilcher et al. 1984
	collision cross sections	-	-	-	3	0[n]	-	-	~⊥ to Io's motion	-	-	-	-	-	Sieveka and Johnson 1984
	nearer zenocorona structure	-	-	~20± 12[p]	-	-	-	-	tangential ± isotropic	photoionization	~400 hr	no	no; Sun yes	yes	Smyth and Combi 1991
	nearer zenocorona structure	-	-	~20± 12[p]	-	-	-	-	tangential ± isotropic	photoionization	~400 hr	no	yes	no	Flynn et al. 1992
	spacetime structure	-	-	20± 10-20[q]	-	-	-	-	tangential ± isotropic	none	∞	no	yes	no	Wilson and Schneider 1995

[a] regarding Io's exobase, L=leading, I=inner, T=trailing, O=outer.
[b] east-west intensity asymmetry data of Bergstralh et al. (1975, 1977).
[c] early (i.e., partial) Na eclipse data set from Schneider et al. (1987).
[d] used cut-off energy: Emin ≤ E < ∞; Emin = k $T_{exobase}$; $T_{exobase}$=1500 K (i.e. a 1.04 km s^{-1} cut-off speed).
[e] complete eclipse data set from Schneider (1988) and Schneider et al. (1991).
[f] two sodium cloud images of Matson et al. (1978).
[g] I-L hemisphere centered 30° longitude (0° longitude facing Jupiter, 90° longitude is the leading point in the orbit).
[h] fifty-six sodium cloud images of Murcray (1978) and Murcray and Goody (1978).
[i] I-T hemisphere centered on -40° longitude.
[j] east-west orbital asymmetry data of Goldberg et al. (1978).
[k] velocity components equally weighted.
[l] distribution parameters from Carlson (1995, private communication); I-L hemisphere centered on 45° longitude.
[m] from images of Pilcher et al. (1984).
[n] used cut-off energy of 0.5 ev (i.e., Na cut-off speed of 2.0 km s^{-1}).
[p] tangential speed to Io's orbit at Io position ± most probable speed of an isotropic Maxwell-Boltzmann.
[q] tangential speed to Io's orbit at Io position ± most probable speed of an isotropic Gaussian.

intensity asymmetry and also the general spatial morphology of the forward sodium cloud, located on a much larger spatial scale well beyond the Lagrange sphere. These studies showed that the sodium ejection speed at the exobase required to fit the east–west intensity asymmetry is double-valued, having a lower value of ≤ 1 km sec^{-1} and a higher value in the range 2.6–3.65 km sec^{-1}. For a Maxwell–Boltzmann flux distribution, the lower and higher most probable speed values were 0.71 km sec^{-1} (T = 460 K) and 3.65 km sec^{-1} (T = 12,300 K). Neither distribution was, however, suitable for properly populating the forward cloud. The lower value produces essentially only ballistic atom orbits which could not populate the forward cloud, while the higher value was significantly larger than the nominal ~2.6 km sec^{-1} characteristic monoenergetic velocity required to reproduce the proper spatial morphology of the forward cloud as a function of the Io geocentric phase angle. For a Maxwell–Boltzmann flux distribution with a more nominal thermal exobase temperature in the range ~1000–2000 K, the calculated east–west intensity ratio was much higher than the observed value, with the atoms still contributing primarily to the corona density and again far too deficient in energy to contribute any significant sodium to the forward cloud. For the preferred (α = 7/3) modified-sputtering distribution of Smyth and Combi (1988b) with source strength ~2×10^{26} atoms sec^{-1}, the lower and higher speed values were ≤ 0.5 and ~2.9 km sec^{-1}, respectively, with the latter value being preferred because of its closer proximity to the ~2.6 km sec^{-1} characteristic velocity for the forward cloud. Interestingly, however, it is actually the lower value that will be shown in this paper to reproduce the correct spatial profile for sodium both within the Lagrange sphere and beyond in the more distant neutral cloud.

2.2. *Corona: Column Density Profile*

In Table I, modeling studies of Smyth and Combi (1987b,c) determined that typical forward cloud brightness data for the sodium cloud could be properly simulated well beyond the Lagrange sphere radius of ~5.81 R_{Io} by a sodium source of ~1×10^{26} atoms sec^{-1} ejected monoenergetically from Io's exobase with a characteristic velocity of ~2.6 km sec^{-1}. They also established that this same sodium source reproduced the column density profile of Schneider *et al.* (1987) within the Lagrange sphere down to a radius of ~3.5 R_{Io}. For a radius smaller than ~3.5 R_{Io}, the calculated profile was lower than the observed profile, indicating that lower (ballistic) velocity components are required, in addition, as part of a more realistic flux velocity dispersion. A similar behavior for the simulated column density profile, with an even more dramatic departure from the observed profile both inside and outside the Lagrange sphere, was also later shown by a model calculation of Ip (1990), who assumed an exobase speed of 3 km sec^{-1} but did not include the gravity of Jupiter so as to properly include the near zero escape speed conditions for sodium at the Lagrange sphere. Adopting for sodium atoms at the exobase a simple (i.e., binding-energy velocity v_b = 0) classical sputtering energy distribution with a low energy cut-off and also excluding Jupiter's gravity, McGrath (1988) modeled the column density within the Lagrange sphere and produced a profile with a slope slightly less steep than the observation for an infinite sodium lifetime and a slope somewhat steeper than the observation for a sodium lifetime of 3 hr. Alternatively adopting a Maxwell–Boltzmann flux distribution, assuming an infinite sodium lifetime, and similarly excluding Jupiter's gravity, Summers *et al.* (1989) and Schneider *et al.* (1991) modeled the column density within the Lagrange sphere region and produced a profile that reasonably well matched the observed profile for an exobase temperature, respectively, of 1000 K based on the partial eclipse data set (Schneider *et al.* 1987) and of 1500 K based on the complete eclipse data set (Schneider *et al.* 1991). Although these different flux velocity distributions reasonably fit the observations within the Lagrange sphere, it is clear from the earlier studies of Smyth and Combi (1988b) that these Maxwell–Boltzmann distributions are energetically deficient and inappropriate for populating the neutral cloud and, furthermore, that the more energetically promising sputtering distribution cannot be investigated adequately near or beyond the Lagrange sphere radius without properly including the gravity of Jupiter, solar radiation acceleration, and the spacetime variable sodium lifetime in the plasma torus. This study will be undertaken in Section 4.

2.3. *Sodium Cloud*

The early studies in Table I for the sodium cloud were general in nature, probing its poorly documented spatial and angular extent about the planet. Based upon the solar resonance scattering excitation mechanism for sodium (Bergstralh *et al.* 1975) and limited angular extent data determined by slit-averaged intensity data, Carlson *et al.* (1975) undertook monoenergetic (3.5 km sec^{-1}) model calculations and estimated that the sodium cloud lifetime (assumed to be spatially uniform) was likely determined by electron impact ionization by the (then very poorly characterized) plasma in the planetary magnetosphere. This general picture for the cloud was confirmed by more extensive model calculations performed by Fang *et al.* (1976) and Smyth and McElroy (1977), the latter of which explored the time evolution and two-dimensional nature of the cloud for exobase velocities near the Io Lagrange escape speed. The acquisition of sodium cloud images in late 1976 and early 1977 brought this subject into dramatic focus. For a classical sputtering flux distribution that peaked at 4 km sec^{-1}, Matson *et al.* (1978) successfully

modeled a one-dimensional east–west brightness profile (derived from a cloud image) which extended from Io in the forward cloud to ~80 R_{Io} and in the trailing cloud to ~40 R_{Io} but which excluded sodium emission within Io's corona. The analysis (Smyth and McElroy 1978) of a much larger sodium cloud image data set (Murcray 1978) also indicated that the forward cloud could be characterized by an exobase ejection speed of ~2.6 km sec^{-1} and that its changing intensity pattern could be understood as the changing viewing perspective of an approximately steady state cloud on the sky plane as Io moved on its orbit around Jupiter. The observed predominance of the forward sodium cloud over the trailing cloud was accomplished in all these models by limiting the exobase source area to a hemisphere (see Table I) and by limiting the assumed spatially uniform lifetime so as to dynamically select sodium atom orbits that would primarily populate the forward cloud. Additional modeling studies by Macy and Trafton (1980) of the radial and vertical cloud structure on a larger spatial scale indicated source dispersion speeds at least up to 13 km sec^{-1} were, however, required to explain a variety of other observations. Additional model studies (Smyth 1979, 1983) showed that the newly discovered east–west orbital asymmetry of the sodium cloud (Goldberg *et al.* 1978) was not source related but was due to the perturbing action of solar radiation acceleration on the sodium atom orbits. Adopting a one-dimensional radially dependent sodium lifetime in the plasma torus based upon limited Voyager spacecraft data and an asymmetric exobase source for a classical sputtering distribution with a peak velocity at 4 km sec^{-1}, Goldberg *et al.* (1980) successfully modeled a one-dimensional east–west brightness profile acquired during the Voyager 1 encounter for distances extending from Io in the forward cloud to ~80 R_{Io} and in the trailing cloud to ~30 R_{Io}. Later modeling by Smyth and Combi (1988b) using a more accurate two-dimensional space- and time-dependent sodium lifetime in the plasma torus and an isotropic (or near isotropic) exobase sodium source of ~2×10^{26} atoms sec^{-1} demonstrated that the predominant forward cloud was caused by the highly radially dependent sink for sodium in the plasma torus and not by a nonisotropic source. The deduced characteristic or most probable exobase speed for the more definitive modeling of the forward sodium cloud above is, therefore, in the range ~2.6 to 4 km sec^{-1} and is much larger than required to characterize the sodium column density profile in Io's corona. A new flux speed distribution is therefore needed for consistency and is determined in Section 4.

2.4. Directional Feature

In Table I, observations acquired in 1980 and 1981 by Pilcher *et al.* (1984) for weaker D-line emissions in the trailing portion of the sodium cloud allowed them to discover an elongated feature in the brightness distribution that on the sky plane was directed away from Jupiter and was inclined sometimes to the north and sometimes to the south of the satellite's orbital plane. The north–south direction of the feature was shown to be correlated with Io's magnetic longitude and suggested a formation mechanism involving the oscillating plasma torus. Modeling analysis by Pilcher *et al.* indicated that the feature resulted from a high-velocity (~20 km sec^{-1}) sodium source that was at near right angles to Io's orbital motion with a source strength required on the outer satellite hemisphere of ~1×10^{26} atoms sec^{-1}. This peculiar directionality of the source was investigated by Sieveka and Johnson (1984), who concluded that it was likely produced by direct collisional ejection of neutral sodium from the exosphere by the corotating plasma flow past Io. Modeling of the sodium zenocorona (Smyth and Combi 1991; Flynn *et al.* 1992) showed that it was consistent with a two-component exobase source: a similar high-velocity (~20 km sec^{-1}) sodium source of ~1×10^{26} atoms sec^{-1} for the spatial distribution nearer the planet and an even higher-velocity (~57 km sec^{-1}) sodium source of ~2×10^{26} atoms sec^{-1} for the spatial distribution further from the planet. Both source components, however, were based on ion–neutral charge exchange processes in Io's exosphere and were hence composed of a speed tangential to Io's orbit at Io's position plus an isotropic Maxwell–Boltzmann distribution with a most probable speed of about one-third of the tangential speed in the Jupiter frame (i.e., one-third of ~37 and ~74 km sec^{-1}, respectively). In Table I, the lower component is therefore symbolically denoted in the Io frame by 20 ± 12 km sec^{-1}. Recent modeling of the directional features has also been reported by Wilson and Schneider (1995), who used a similar lower component source denoted in Table I by $20 \pm$ 10–20 km sec^{-1}, where the isotropic portion of their source may be variable in magnitude. A spatially distributed molecular-ion source has also been used to model the sodium zenocorona (Flynn 1993), but appears to be of secondary importance due to its smaller source rate and erratic presence.

3. OBSERVATIONAL DATA BASE FOR MODELING

To describe the entire spatial distribution of sodium in Io's corona and beyond in the extended neutral clouds, three different types of sodium observations obtained on very different spatial scales are combined. For Iocentric distances, the combined data set is composed of the novel 1985 eclipse measurements of Schneider *et al.* (1991) acquired from ~1.4 to ~10 R_{Io}, the 1985 east–west emission data of Schneider *et al.* (1991) acquired from ~4 to ~40 R_{Io}, and sodium cloud image data acquired near Io's orbital plane from ~10 to ~100 R_{Io} by a number of different

TABLE II
Io Eclipse and Emission Observations for 1985

Date	UT Midpoint	Io Geocentric Phase Angle Range (deg)	Io System III Longitude Range (deg)	Spectrum ID	Type of Observation		Dominant Spatial Profile	Directional Feature Orientation	Enhance Doppler Signature	D_2 Emission Profile Power Law Fit [f] Exponent		Amplitude (kR)	
					Eclipse	Emission				East Profile	West Profile	East Profile	West Profile
August 27	0714	61.4 ± 0.7	29.9 ± 2.3	85g188		1	forward	null	trailing/forward	1.67 (F)	1.57 (T)	191	124
	0720	62.3 ± 11.0	32.9 ± 35.8	a	1		---	---	---				
	0830	72.2 ± 1.1	65.1 ± 3.4	85g196		2	symmetric	south	no	1.85 (S)	1.80 (S)	169	142
September 13	0641	276.6 ± 0.7	194.7 ± 2.3	85h032		3	trailing	null/north	trailing	---	---	---	---
September 14	0245	87.7 ± 0.7	31.4 ± 2.3	85h102		4	trailing	null	trailing	1.23 (S/T)	1.80 (S/F)	89	188
	0326	93.5 ± 4.2	50.5 ± 13.7	b	2		---	---	---				
	0416	100.6 ± 0.4	73.6 ± 1.4	85h113		5	g	south	no	1.27 (T)	---	66	---
September 15	0316	294.7 ± 0.7	353.7 ± 3.0	85h152		6	trailing	null	trailing	---	---	---	---
	0500	309.4 ± 11.5	41.7 ± 37.4	c	3		---	---	---				
September 21	0604	100.5 ± 1.6	112.5 ± 5.2	d	4		---	---	---				
September 23	0230	117.2 ± 0.7	267.6 ± 2.3	85h433		7	forward	north	no	2.05 (T)	1.57 (F)	342	135
	0301	121.6 ± 0.4	281.9 ± 1.2	85h436		8	forward	north	no	1.96 (T)	1.54 (F)	283	138
	0356	129.3 ± 2.0	307.3 ± 6.7	e	5		---	---	---				
	0534	143.1 ± 0.7	352.9 ± 2.3	85h457		9	forward	null	no	2.16 (T)	1.64 (F)	374	165

a. Eclipse 1 : 85g179, 85g181, 85g185, 85g188, 85g192, 85g193, 85g196

b. Eclipse 2 : 85h103, 85h104, 85h105, 85h106, 85h107, 85h108, 85h109, 85h110, 85h112

c. Eclipse 3 : 85h153, 85h154, 85h155, 85h157, 85h159, 85h162, 85h163

d. Eclipse 4 : 85h287, 85h288, 85h289, 85h290, 85h291, 85h292, 85h293, 85h294, 85h295

e. Eclipse 5 : 85h441, 85h442, 85h443, 85h444, 85h445, 85h446, 85h447, 85h448, 85h449, 85h450

f. Profile points inside of 4 R_{Io} are excluded; power law fit $A\,r^{\beta}$, where A is the amplitude, β is the exponent, and r is in units of R_{Io}; F = forward cloud; S = symmetric turning point; T = trailing cloud.

g. Not sufficient data west of Io to compare spatial profils (see Table III).

(Note one lower-bound data point from eclipse 4 at a distance from the center of Io of 1.17 R_{Io} is excluded in the analysis since it is well within the nominal exobase radius of 1.4. R_{Io})

observers in the 1976 to 1983 time frame. For modeling purposes in Section 4, a one-dimensional east–west profile centered on Io is constructed from this data set. From the data of Schneider *et al.* (1991), five higher quality eclipse profiles and nine higher quality emission profiles have been selected, and their observational dates, times, Io angular parameters, spectral ID numbers, and the numbering of these interleaved observations as adopted in this paper are summarized in Table II. The D_2 brightnesses for the emission profiles in Table II, previously published only in a graphical format, are given numerically in Table III as provided by Schneider (1990, 1995, both private communications). For the sodium cloud data, fourteen images in the D_2 emission line acquired in the 1976–1983 time interval (Murcray 1978; Murcray and Goody 1978; Matson *et al.* 1978; Goldberg *et al.* 1980, 1984; Morgan 1984, private communication) have been selected, with values for the east–west D_2 brightness profiles of the forward and trailing clouds extracted and summarized in Table IV.

The eclipse observations provide the most accurate information in the radial interval from ~1.4 to 6 R_{Io} for the atomic sodium column density profile in the corona within the Lagrange sphere of Io (i.e., a radius of 5.81 R_{Io}) and yield an essentially symmetric column density profile about Io with a power law fit $N\ (1.4 \le r \le 5.85) = 2.55 \times 10^{12} r^{-2.48}$, where N is in units of atoms cm^{-2} and r is the distance from the Io's center in units of R_{Io}. This power law fit, however, undercuts the eclipse data beyond the Lagrange radius, and this reduced slope will later be seen to be caused by the dominant planetary gravitational field beyond Io's Lagrange radius. The emission observations provide accurate information for the sodium D_2 brightness from just within the Lagrange sphere outward into the nearer portion of the sodium cloud (i.e., ~4–40 R_{Io} from Io's center) with a power law fit $I_{D_2}(r \ge 4) = 101\ r^{-1.45}$, where I_{D_2} is in units of kiloRayleighs (kR) and where the D_2 brightness of ~100 kR as r approaches Io's surface is consistent (see Brown and Yung 1976) with the maximum sodium column density of $\sim 1 \times 10^{12}$ atoms cm^{-2} deduced from the eclipse data. The brightnesses for the different observed profiles in Table III, however, vary by a factor of ~3 to almost 5 at the same distance from Io but have error bars that are no larger than ±30%, suggesting that the large variation is real and likely correlated with Io geocentric phase angle, Io System III longitude, and the east–west asymmetry in the plasma torus, as is the case for sodium cloud image data. The closer spatial regions covered by the eclipse data and the near Io emission data are, however, masked in the cloud images by a circular (or nearly circular) occulting mask of ~10 R_{Io} in radius centered on Io. The sodium cloud image data in Table IV, as illustrated in Fig. 1, hence contribute to the east–west brightness profiles for Iocentric distances from ~10 to ~100 R_{Io}.

The structure of the sodium cloud emission brightness on the sky plane has been historically divided into a forward cloud, so-called because it appears ahead of the satellite in its orbit (i.e., in Fig. 1 located right (west) of Io in image A and left (east) of Io in images B and C), and a corresponding trailing cloud that appears behind the

TABLE III
Emission Data for 1985

	Radial Distance From Io (satellite radii)	D_2 Intensity‡(kR) Emission 1 61.4° 27 August (85g188)	Emission 2 72.2° 27 August (85g196)	Emission 4 87.7° 14 September (85h102)	Emission 5 100.6° 14 September (85h113)	Emission 7 117.2° 23 September (85h433)	Emission 8 121.6° 23 September (85h436)	Emission 9 143.1° 23 September (85h457)	Emission 3* 276.6° 13 September (85h032)	Emission 6 294.7° 15 September (85h152)
	-29.92					0.69 ± 0.17	0.93 ± 0.18	0.66 ± 0.16		
	-29.65									1.12 ± 0.19
	-24.48								1.40 ± 0.21	
	-21.76					1.19 ± 0.19	0.84 ± 0.17	0.95 ± 0.18		
	-16.32					1.38 ± 0.20	2.10 ± 0.26		2.22 ± 0.27	
	-15.78							1.74 ± 0.23		2.15 ± 0.26
	-14.96				1.91 ± 0.24					
	-10.88	3.16 ± 0.35				2.90 ± 0.33	3.29 ± 0.36	3.38 ± 0.37	4.40 ± 0.46	
↑	-9.52			3.17 ± 0.35						
West	-6.80	5.21 ± 0.54	4.50 ± 0.47	6.41 ± 0.66		7.49 ± 0.76	7.76 ± 0.79		11.54 ± 1.16	
	-4.08	14.65 ± 1.47	11.29 ± 1.14	14.71 ± 1.48				7.54 ± 0.77	28.69 ± 2.87	
	-3.81									18.75 ± 2.63
	-2.18	24.31 ± 3.40	18.39 ± 2.57	24.12 ± 3.38		25.61 ± 3.59	25.01 ± 3.50	21.00 ± 2.94	45.47 ± 6.37	
	-1.09	27.46 ± 3.84	19.99 ± 2.80	27.14 ± 3.80		29.95 ± 4.19	28.72 ± 4.02	23.89 ± 3.34	48.61 ± 6.81	
	-0.82									24.85 ± 3.48
Io	0.00	27.44 ± 3.84	19.19 ± 2.69	27.14 ± 3.80		27.90 ± 3.91	30.16 ± 4.22	23.97 ± 3.36	45.56 ± 6.38	
	0.27									25.27 ± 3.54
	1.09	25.87 ± 3.62	19.35 ± 2.71	26.65 ± 3.73	23.03 ± 3.22	26.31 ± 3.68	26.39 ± 3.69	22.84 ± 3.20	39.45 ± 5.52	
	1.36									22.90 ± 3.21
	2.18	25.19 ± 3.53	16.87 ± 2.36	25.68 ± 3.60	19.60 ± 2.74	22.42 ± 3.14	23.91 ± 3.35	20.21 ± 2.83	33.60 ± 4.70	
	3.26									11.53 ± 1.61
	4.08	17.60 ± 1.77	11.92 ± 1.20	18.10 ± 1.82	11.87 ± 1.20	15.54 ± 1.56	14.83 ± 1.49	12.52 ± 1.26	20.06 ± 2.01	
	5.98									4.79 ± 0.50
East	6.80	8.31 ± 0.84	5.52 ± 0.57	8.17 ± 0.83	5.52 ± 0.57	7.09 ± 0.72	7.10 ± 0.73	6.02 ± 0.62	7.52 ± 0.77	
↓	10.06									1.66 ± 0.22
	10.88	3.40 ± 0.37	1.94 ± 0.25	3.84 ± 0.41	3.21 ± 0.35	2.47 ± 0.29	2.47 ± 0.29	2.26 ± 0.27	2.73 ± 0.31	
	15.50									0.77 ± 0.17
	16.32			2.84 ± 0.32	1.81 ± 0.24	1.03 ± 0.18	1.11 ± 0.19	0.82 ± 0.17	1.39 ± 0.20	
	21.76			2.25 ± 0.27		0.68 ± 0.16	0.75 ± 0.17	0.52 ± 0.16		
	23.66									0.53 ± 0.16
	24.48				1.24 ± 0.19				1.06 ± 0.18	
	27.20			1.39 ± 0.21						
	35.36			1.27 ± 0.20					1.00 ± 0.18	
	46.24								0.83 ± 0.17	

‡Nonuniform spatial coverage occurs because of different distance intervals adopted to obtain good average brightness values (given different signal to noise ratios) and because of signal drop-out associated with constraints imposed on positioning the slit profile on the CCD detector during interleaved eclipse and emission measurements.
*Calibration uncertain

TABLE IV
East–West D_2 Brightness Profiles for Sodium Cloud Image Data

UT Date	UT Time	Image ID Number	Io Geocentric Phase Angle (deg)	Io System III Longitude (deg)	East-West Distance from Io for Specified D_2 Brightness Level (satellite radii)							
Image Data Set Reference: Murcray (1978)					0.5 kR		1.0 kR		1.5 kR		2.0 kR	
					Forward	Trailing	Forward	Trailing	Forward	Trailing	Forward	Trailing
1976 Nov. 16	0806	ES 328B	256	262	--	--	51	29	46	24	28	14
1977 Jan 27	0024	ES 369A	86	193	60	38	50	22	44	19	32	16
	0217	ES 370D	102	245	>83	30	56	25	46	21	24	19
Image Data Set Reference: Goldberg(1988†)					0.2 kR		0.5 kR		1.0 kR		2.0 kR	
					Forward	Trailing	Forward	Trailing	Forward	Trailing	Forward	Trailing
1981 May 5	0819	SIP 418/31-33	102	300	78	69	63	40-66	45	37	24	21
May 12	0848	SIP 420/30-32	91	302	66	86	41	37	35	29	20	21
May 13	0346	SIP 421/21-23	253	108	74-103	73	70	41	41	27	29	20
	0555	SIP 421/32-33	271	168	124	65	112	44	51	30	26	19
June 6	0436	SIP 424/10-12	103	300	81	75	68	71	36	26	20	23
Image Data Set Reference: Morgan (1984†)					0.3 kR		0.6 kR		0.9 kR		1.8 kR	
					Forward	Trailing	Forward	Trailing	Forward	Trailing	Forward	Trailing
1983 June 13	0714	i 8492	274	230	--	39	58	26	37	19	20	--
	0722	i 8494	275	233	--	35	52	22	40	20	20	--
	0729	i 8496	276	237	>93	36	52	22	37	17	22	--
	0827	i 8501	284	264	>93	39	61	25	42	19	23	--
	0949	i 8509	296	301	>93	47	63	26	44	17	24	--
	1010	i 8511	299	311	>93	41	63	23	44	16	19	--

†Image observational data obtained by private communication.

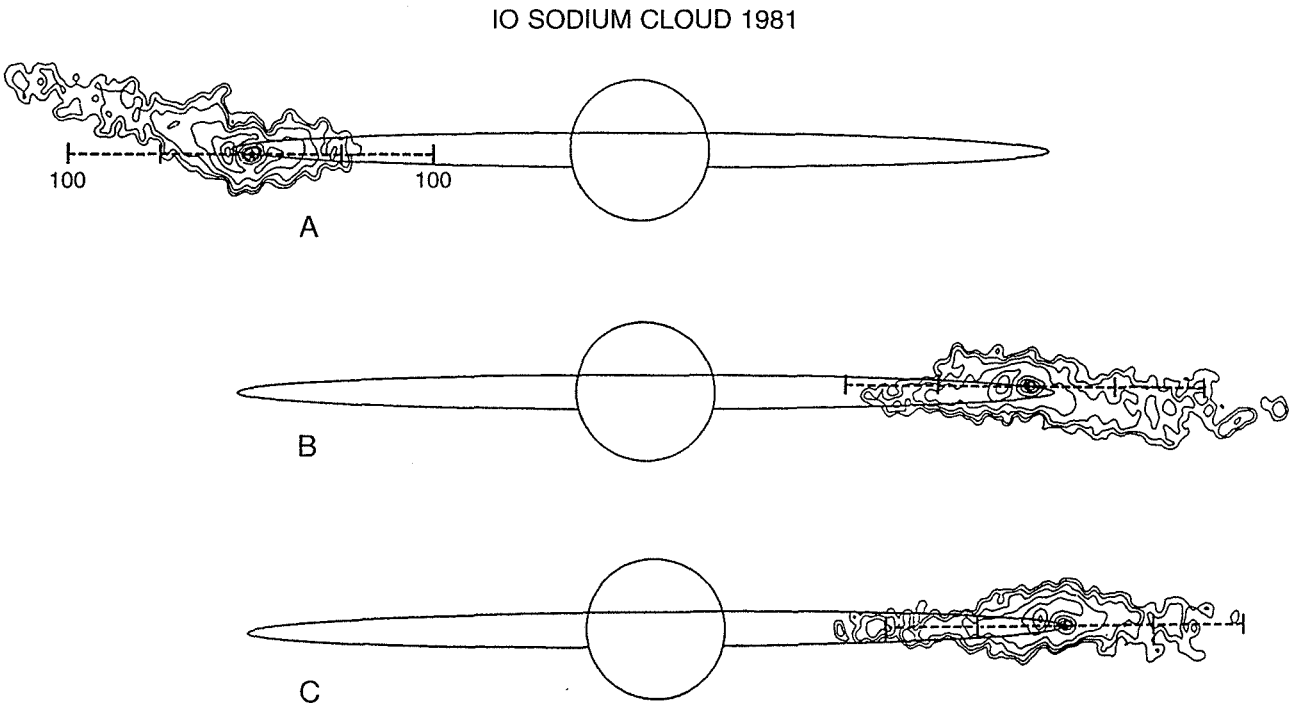

FIG. 1. Io sodium cloud images. Three calibrated D_2 emission images of the Io sodium cloud from the JPL Table Mountain Data Set are shown to proper scale with Jupiter and Io's orbit as viewed from earth in 1981 (Smyth and Goldberg 1993). The Io System III longitude and corresponding orientation of the trailing directional feature in image A are 247° and north, in image B are 104° and south, and in image C are 178° and only very slightly north. An east–west spatial scale of ±100 satellite radii about Io is shown for reference, with tick marks also located at ±50 satellite radii. Contour levels for the D_2 brightness, from outside to inside, are 0.2, 0.5, 1, 2, 4, 6, 8, and 10 kR. An occulting mask of ~10 R_{Io} in radius is centered on Io so that brightness values within this distance are not accurate.

satellite. The forward cloud changes in length, brightness, and east–west orientation relative to the satellite's location as Io moves about Jupiter (i.e., as a function of the Io geocentric phase angle). This change in orientation is well documented (Murcray 1978; Murcray and Goody 1978; Goldberg *et al.* 1984) and is due primarily to the projection upon the two-dimensional sky plane of a three-dimensional cloud (Smyth and McElroy 1978), slightly altered from mirror symmetry by solar radiation pressure (Smyth 1979, 1983), which passes through an east symmetric turning point between about 65° and 85° to 90° and a west symmetric turning point at about 235° (Goldberg *et al.* 1984). A detailed examination of the emission data of Schneider *et al.* (1991), summarized in the last seven columns of Table II, shows that the forward and trailing profiles for the emission data are quite consistent with this known behavior of the Io sodium cloud images. In the trailing cloud, the time-dependent change in the north–south inclination of the fainter directional feature (see Fig. 1) has been shown to be correlated with the System III longitude of Io (Pilcher *et al.* 1984; Goldberg *et al.* 1984) with the directional feature changing from a south to north inclination (a first null point) at an Io System III longitude near 165° and changing from a north to south inclination (a second null point) for a rather poorly defined Io System III longitude somewhere between about 320° and 25°. When the directional feature is near the null location, as illustrated in Fig. 1, an increase in both the spatial extension and brightening of the trailing cloud along the east–west oriented (dashed) line is readily apparent. In addition, since the trailing cloud is associated with a high-speed Io sodium source (~15–20 km sec^{-1}), an increase in the Doppler width of the spectral line in the trailing cloud brightness along an east–west slit is also expected near the null location and is indeed observed in the emission data of Schneider *et al.* (1991), as indicated in Table II.

Information for the sodium D_2 brightness profiles in both the forward and trailing clouds is presented in Fig. 2. The forward and trailing cloud orientation depicted in Fig. 2 is chosen for Io near eastern elongation in order to facilitate the comparison with the 1985 emission data profiles, mostly acquired for Io east of Jupiter. The five emission profiles of Schneider *et al.* (1991) for Io east of Jupiter are shown by different symbol together with their power-law fits ($I_{D_2}(r \geq 4) = Ar^{-\beta}$) given in Table II. For the Io sodium cloud images, the extracted east–west D_2 brightness profiles in Table IV for the forward and trailing clouds are shown by shaded areas, which represent appro-

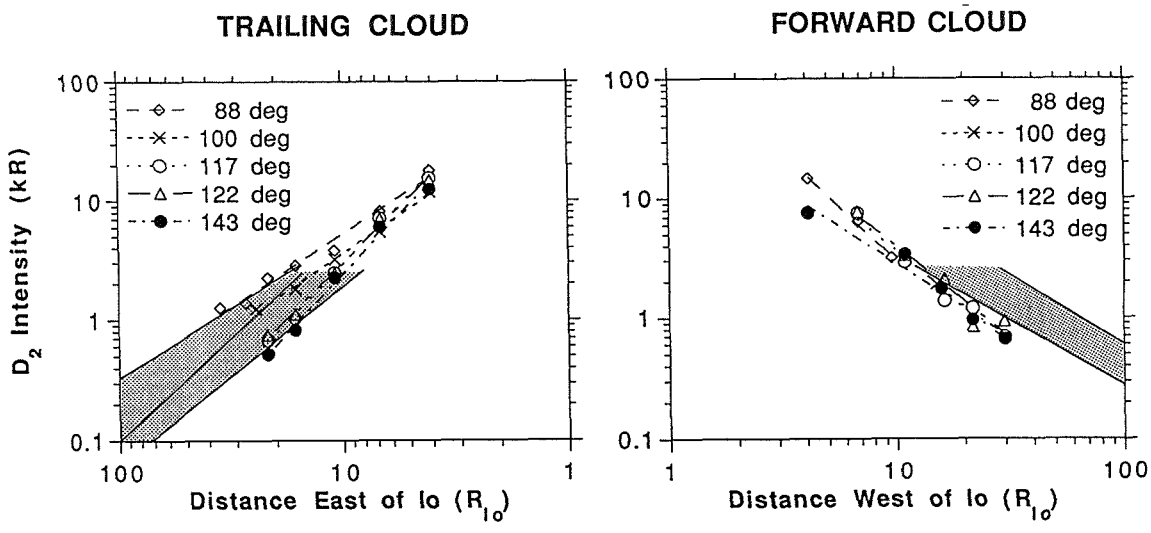

FIG. 2. East and west brightness profiles for selected 1985 emission data and image cloud data. The spatial profiles both east and west of Io for the sodium D_2 emission brightness in units of kilorayleighs are shown as a function of the distance along the observing slit from the center of Io. Five emission observations identified by their satellite geocentric phase angles are shown by the different symbols. These five profiles occur when Io is east of Jupiter and past the satellite phase angle where the forward cloud has its symmetric turning point so that the trailing cloud profiles are all to the east (left) of Io and the forward cloud profiles are all to the west (right) of Io. A power law fit to each profile is also shown. At larger distances from Io, an envelope for the east–west D_2 emission profile acquired from sodium image data is shown by the shaded area. For the trailing profile, the shaded area is divided into two parts: the lower area corresponding to sodium cloud data when the directional feature is oriented either north or south and the upper area corresponding to the directional feature oriented along the east–west direction (i.e., the null condition).

priate bounds for the brightness profiles when Io is somewhat near the elongation points of its orbit. For the trailing cloud, two different shaded areas are shown in Fig. 2 for the two different basic orientations of the directional feature: (1) lower area, when the directional feature is inclined either north or south, and (2) upper area, when the directional feature is at or near the null locations. As expected, the shaded area for the directional feature near the null locations is both brighter and less steep than the shaded area for the directional feature with either a significant north inclination or a significant south inclination. At larger distances from Io (>30 R_{Io}), however, note that both shaded areas for the trailing sodium cloud are dimmer and more closely confined to Io than the shaded area for the forward cloud. In the forward cloud, all the emission brightness profiles are fairly tightly confined and have a slightly steeper slope than the shaded area due to increasing Io geometric plase angle. In the trailing cloud, the brightest and least steep of these profiles is for the emission 4 (Io phase angle 87.7°) acquired for the directional feature at the null condition, while the next brightest profile is for the emission 5 (Io phase angle 100.6°), acquired ~1.5 hr later.

4. ANALYSIS OF THE OBSERVATIONS

Modeling analysis of the one-dimensional sodium distribution described in the previous section will now be undertaken. Collectively, the eclipse measurements for the corona near Io, the emission measurements that extend into the near sodium cloud, and the sodium cloud image derived profiles that reach to distances of $\pm 100\ R_{Io}$, provide a set of spatially overlapping observations that will be used to study and constrain the initial velocity dispersion of the sodium source atoms at the exobase. In the modeling analysis, one-dimensional profiles are calculated using the numerical sodium cloud model of Smyth and Combi (1988a,b), where the electron impact ionization sink for sodium is determined for a 7° tilted corotating plasma torus with an offset-dipole planetary magnetic field in the presence of a nominal (i.e., ~2.8 mV m^{-1} in Io's frame) east–west electric field. A System III longitudinal asymmetry, although present in the torus ion emission, is not included but deferred to a later time when the electron dependence is available.

To investigate the nature of the initial velocity dispersion of the sodium source, two different source flux speed distributions discussed earlier by Smyth and Combi (1988b; see their Appendix D) are considered: (1) a Maxwell–Boltzmann flux distribution and (2) a modified-sputtering flux distribution. The Maxwell–Boltzmann flux distribution $\phi(v; T)$ is based on the Maxwell–Boltzmann velocity distribution and is defined as

$$\phi(v; T) = \phi_0 \left(\frac{R_S}{R_E}\right)^2 \frac{2}{v_T} \left(\frac{v}{v_T}\right)^3 e^{-(v/v_T)^2} \qquad (1)$$

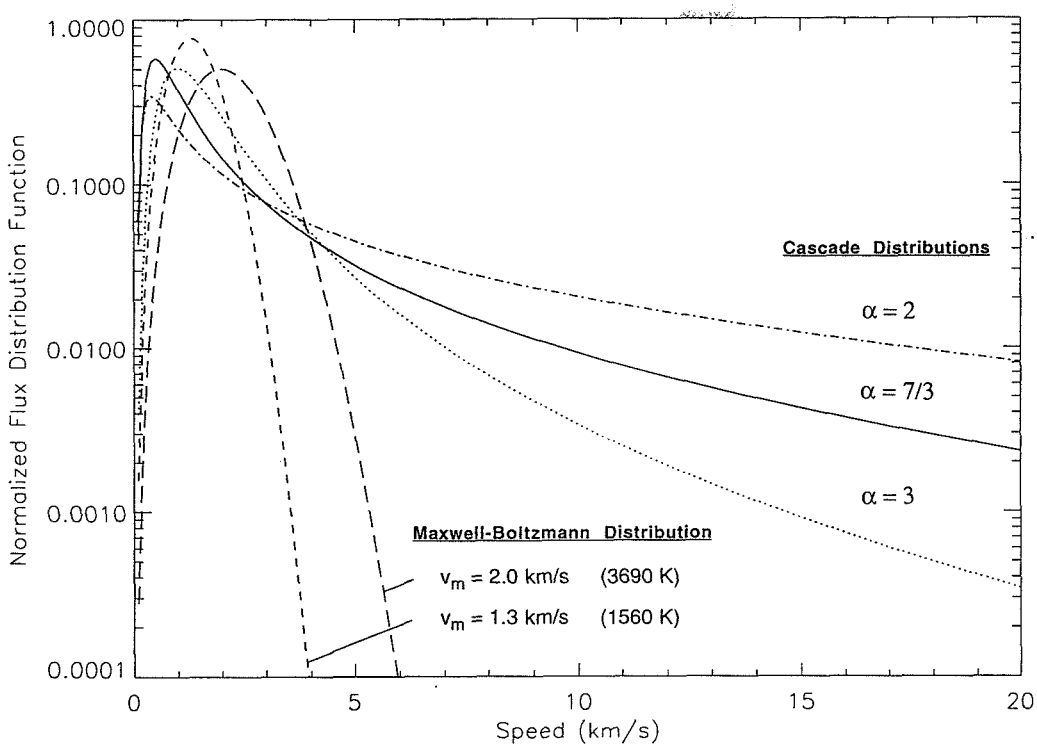

FIG. 3. Flux speed distribution functions for sodium at Io's exobase. Maxwell–Boltzmann flux speed distributions for sodium are shown for most probable speeds, v_m, of 1.3 km sec^{-1} and 2.0 km sec^{-1}. Modified sputtering flux speed distributions are also shown for $\alpha = 3$ and a most probable speed of 1.0 km sec^{-1}, for $\alpha = 7/3$ and a most probable speed of 0.5 km sec^{-1}, and for $\alpha = 2$ and a most probable speed of 0.4 km sec^{-1}. All of the flux speed distributions are normalized to unit area under the curve.

where $v_T = \sqrt{2kT/m}$ is the most probable speed of the velocity distribution for an atom of mass m. The Maxwell–Boltzmann flux distribution is proportional to the local velocity integrated flux ϕ_0 referenced here to the satellite radius R_S not the exobase radius R_E and depends upon one parameter, the exobase temperature T (or alternatively v_T), which determines both the most probable speed $v_m = \sqrt{3kT/m}$ and the speed dispersion of the flux distribution. The modified-sputtering flux distribution $\phi(v; \alpha, v_b, v_M)$ is proportional to the local velocity integrated flux ϕ_0 and depends upon three parameters, an exponent α and two velocity parameters v_b and v_M,

$$\phi(v;\alpha,v_b,v_M) = \phi_0\left(\frac{R_S}{R_E}\right)^2 \frac{1}{v_b D(\alpha, v_M/v_b)}\left(\frac{v}{v_b}\right)^3 \left(\frac{v_b^2}{v^2+v_b^2}\right)^\alpha \left[1-\left(\frac{v^2+v_b^2}{v_M^2}\right)^{1/2}\right], \quad (2)$$

where $D(\alpha, v_M/v_b)$ is a normalization constant (see Smyth and Combi 1988b). The exponent α primarily determines the dispersion of the distribution, which has a greater high-speed population as α decreases. The exponent α has a value of 3 for a classical sputtering distribution (i.e., a complete collisional cascade process) and a value of 7/3 for a Thomas–Fermi modified-sputtering flux distribution (i.e., the limit of a single elastic collisional ejection process), where the latter distribution is based upon a Thomas–Fermi differential scattering cross section. The velocity parameter v_b is related nonlinearly to the most probable speed v_m of the flux speed distribution and primarily determines v_m (see Smyth and Combi, 1988b, Appendix D). The velocity parameter v_M primarily determines the maximum speed for the flux distribution and depends upon the maximum relative speed (and masses) of the plasma torus ion and sodium atom. For different values of their parameters, two Maxwell–Boltzmann flux distributions and three modified-sputtering flux distributions are shown in Fig. 3 and will be utilized in the subsequent modeling analysis.

In calculating the column density and the D_2 emission brightness in the numerical sodium cloud model, a smaller two-dimensional sky-plane grid centered on Io ($\pm 15\ R_{Io}$) is used to cover a spatial scale near the satellite more appropriate to the eclipse data while a much larger two-dimensional sky-plane grid centered on Io is used to cover a larger spatial scale more appropriate for the emission data and the sodium cloud image data. A one-dimensional profile for the eclipse data is obtained from the smaller

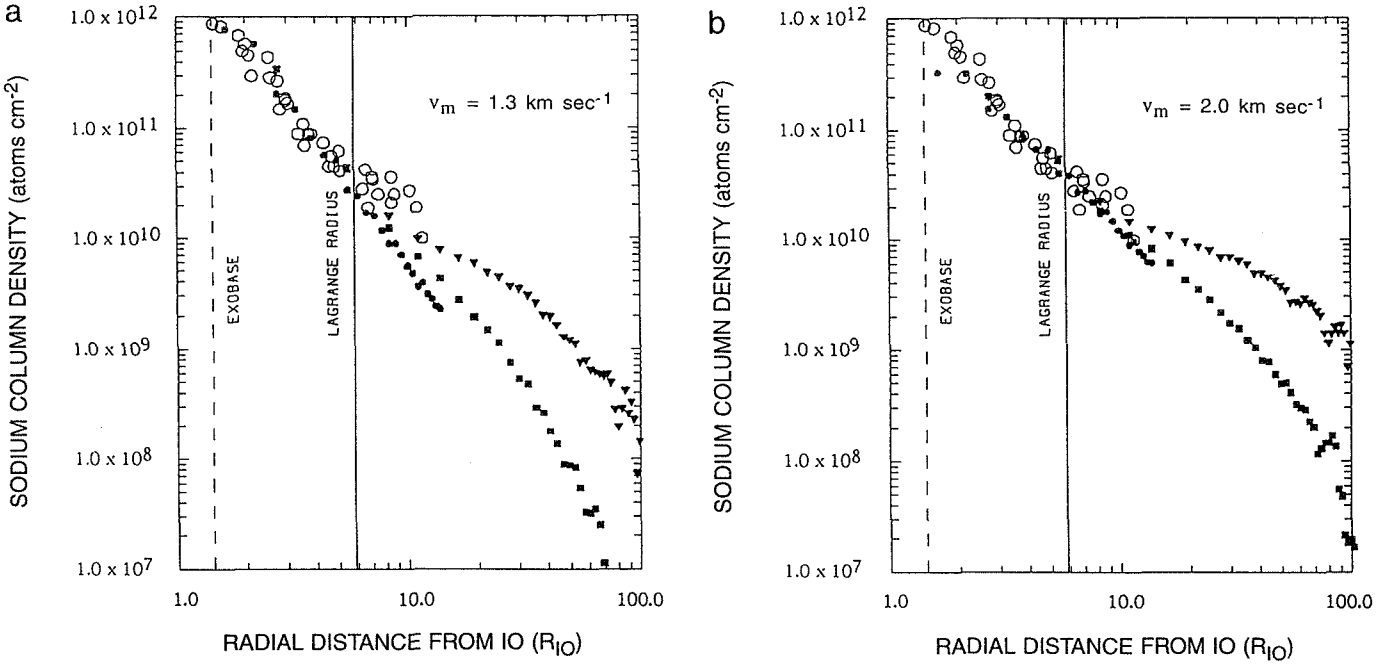

FIG. 4. Model calculations for the Io eclipse data using a Maxwell–Boltzmann flux speed distribution. The atomic sodium column density profile near Io determined from the 1985 eclipse data by Schneider *et al.* (1991) is shown by the open circles. The model calculated column density profiles are shown by solid dots for the (cylindrically averaged) corona, by solid triangles for the forward cloud along the east–west slit direction, and by solid squares for the trailing cloud along the east–west slit direction. These column density profiles were calculated using the Io sodium cloud model of Smyth and Combi (1988b) for their case C description of the plasma torus and for an Io geocentric phase angle of 92.9° and an Io System III longitude angle of 48.6°, which are similar to the emission 4 observation conditions in Table II. Sodium was ejected uniformly from an assumed exobase of 2600 km radius with a velocity dispersion for a Maxwell–Boltzmann flux distribution, where in (a) v_m = 1.3 km sec^{-1} and ϕ_0 = 3.0 × 10^8 atom cm^{-2} sec^{-1}, and in (b) v_m = 2.0 km sec^{-1} and ϕ_0 = 1.8 × 10^8 atom cm^{-2} sec^{-1} (see text).

two-dimensional sky-plane grid by extracting an average radial profile. This average radial profile (called the calculated eclipse profile) will be denoted by the filled circles in Figs. 4–7. A one-dimensional east–west D_2 brightness profile (and also a corresponding column density profile) for the emission data and the sodium cloud image data is obtained from the larger two-dimensional sky-plane grid by selecting only the east–west grid elements that occur in the grid row containing Io. In Figs. 4–7, the calculated east–west brightness and column density profiles are denoted by filled triangles for the forward cloud profile and by filled squares for the trailing cloud profile. To construct an eclipse or east–west profile, monoenergetic model calculations are performed for 18 different nonuniformly spaced speeds ranging from 0.4 to 10 km sec^{-1}. Profiles for speeds beyond 10 km sec^{-1} are determined by an inverse speed extrapolation of the model results. The individual profiles for the different speeds are appropriately weighted for a given source flux speed distribution and then added to obtain the final profile. Model calculations are performed for an Io geocentric phase angle of 92.9° and an Io System III longitude angle of 48.6°. These satellite conditions are similar to those for the emission 4 and eclipse 2 observations of Table II, which are the observations closest to the eastern elongation point. This choice is also appropriate for all the eclipse data, which has no discernible dependence on these two Io related angles, and for the Io sodium cloud image data which have east–west profile areas in Fig. 2 that are representative of the satellite near its orbital elongation points. Modeling analysis results are summarized in Table V and discussed below.

For the first Maxwell–Boltzmann flux distribution in Fig. 3 with a most probable speed of v_m = 1.3 km sec^{-1} (i.e., an exobase temperature of ~1560 K) and with a flux ϕ_0 of 3.0 × 10^8 atoms cm^{-2} sec^{-1} (i.e., a total source of ~1.2 × 10^{26} atoms sec^{-1}), the model calculated eclipse profile (filled circles) in Fig. 4a provides an excellent fit within the Lagrange sphere to the eclipse observations (open circles) and also compares very favorably with the east–west column density profiles calculated for the forward (filled triangle) and trailing cloud (filled squares). This fit verifies and is similar to the earlier 1500 K Maxwell–Boltzmann flux distribution fit of Schneider *et al.* (1991) noted in Section 2. Beyond the Lagrange sphere in Fig. 4a, however, all three of these calculated profiles fall below the eclipse observations, which is considered less accurate

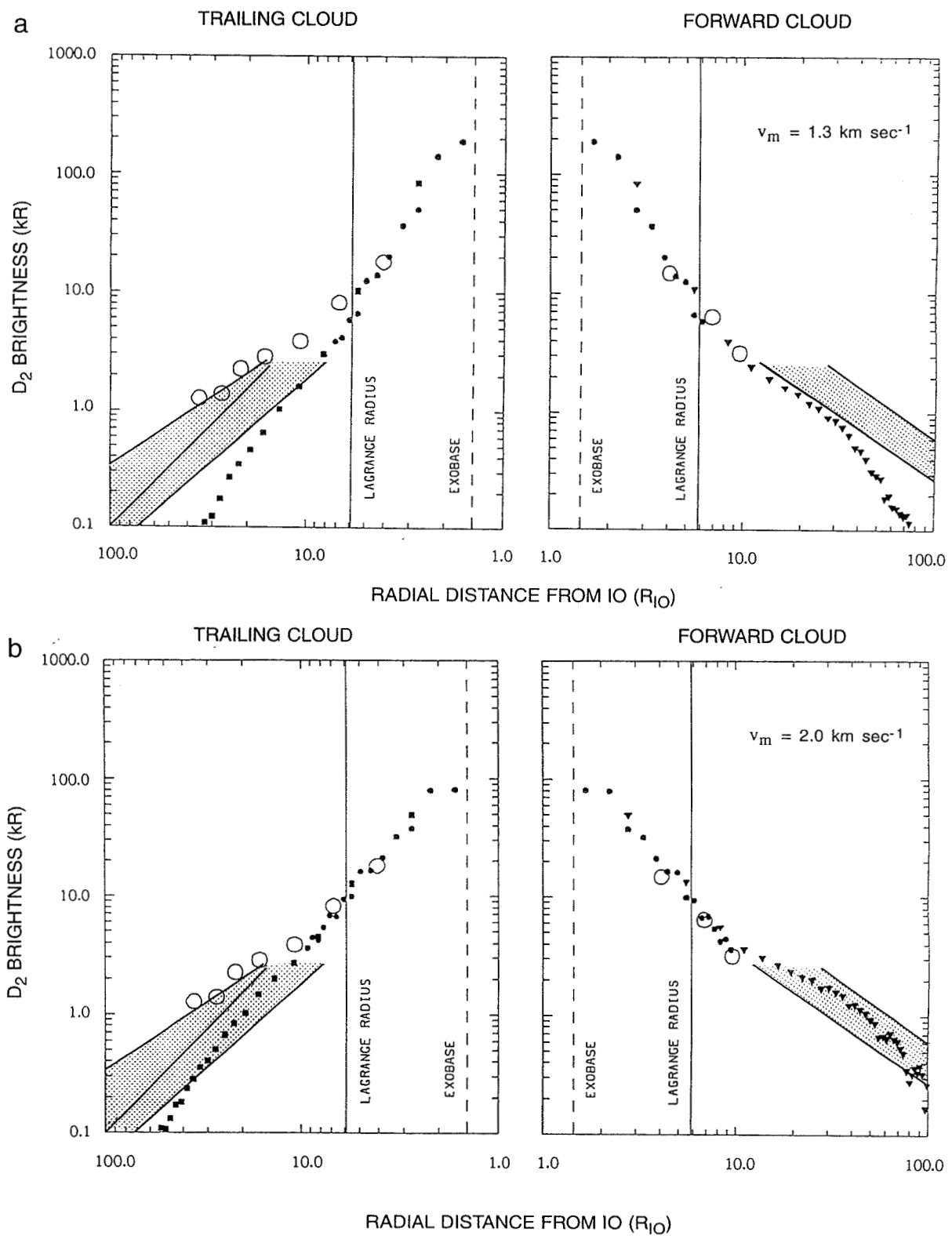

FIG. 5. Model calculations for the east–west D_2 brightness profiles using a Maxwell–Boltzmann flux speed distribution. The east–west D_2 brightness profiles near Io in both the trailing and forward cloud directions as determined by the emission 4 data of Schneider *et al.* (1991) are shown by the open circles. The east–west profile envelopes in both the trailing and forward cloud directions as determined from the sodium cloud image data are shown by the shaded areas (see Fig. 2 caption). The descriptions for the calculated profile symbols, the sodium cloud model and plasma torus, and the Maxwell–Boltzmann flux distribution in (a) and (b) are the same as in the caption of Fig. 4.

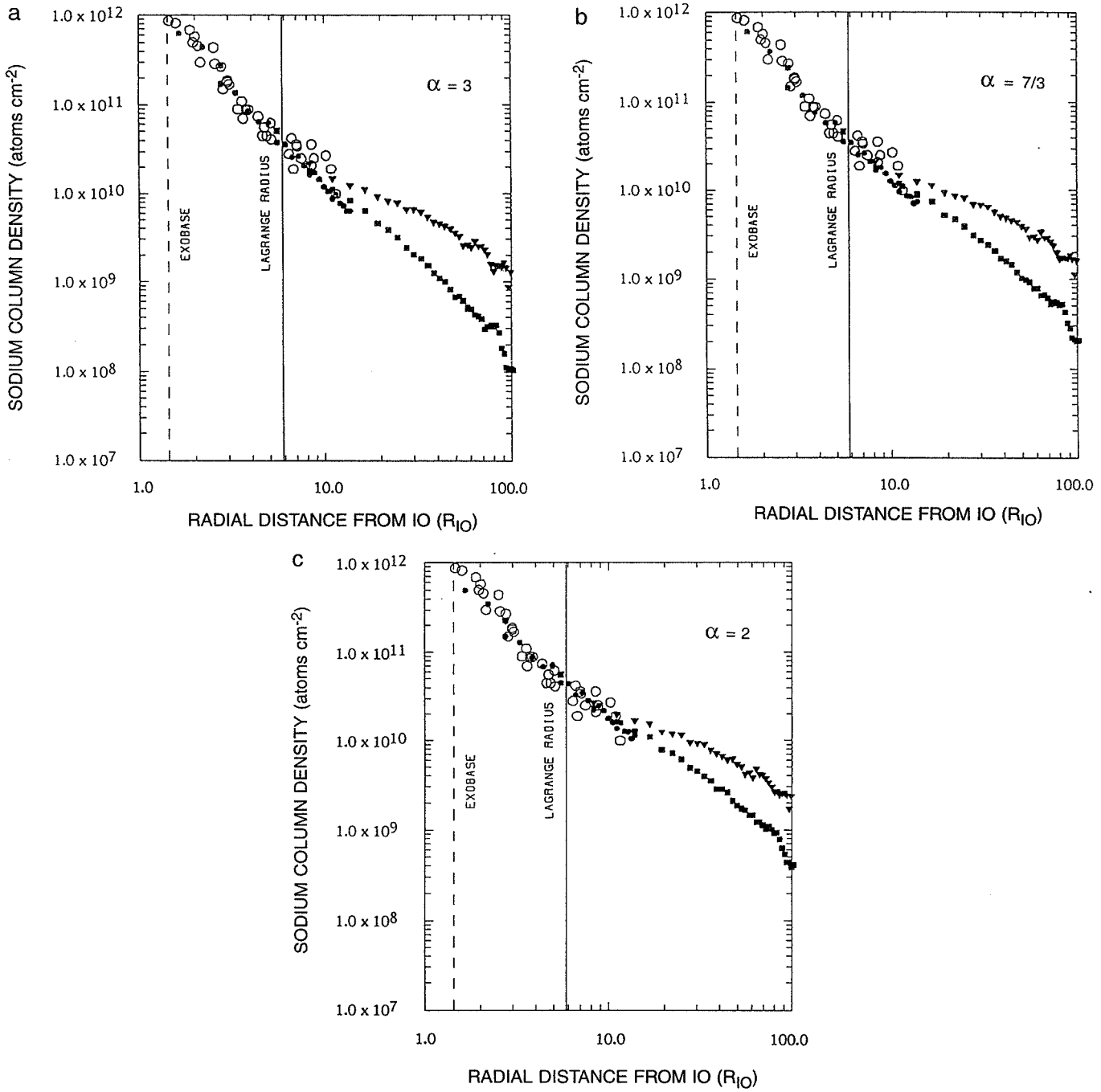

FIG. 6. Model calculations for the eclipse data using a modified sputtering flux speed distribution. The atomic sodium column density profile near Io determined from the 1985 eclipse data by Schneider *et al.* (1991) is shown by the open circles. The model calculated column density profiles are shown by solid dots for the (cylindrically averaged) corona, by solid triangles for the forward cloud along the east–west direction, and by solid squares for the trailing cloud along the east–west direction. These column density profiles were calculated using the Io sodium cloud model of Smyth and Combi (1988b) for their case C description of the plasma torus and for an Io geocentric phase angle of 92.9° and an Io System III longitude angle of 48.6°, which are similar to the emission 4 observation conditions in Table II. Sodium was ejected uniformly from an assumed exobase of 2600 km radius with a velocity dispersion for a modified sputtering flux distribution, where in (a) $\alpha = 3$, $v_m = 1.0$ km sec^{-1}, and $\phi_0 = 3.2 \times 10^8$ atom cm^{-2} sec^{-1}, in (b) $\alpha = 7/3$, $v_m = 0.5$ km sec^{-1}, and $\phi_0 = 4.2 \times 10^8$ atom cm^{-2} sec^{-1}, and in (c) $\alpha = 2$, $v_m = 0.4$ km sec^{-1}, and $\phi_0 = 4.7 \times 10^8$ atom cm^{-2} sec^{-1}.

at these distances. At and beyond about 8 R_{Io}, the calculated east–west forward (filled triangle) and trailing (filled squares) profiles rise above the calculated eclipse profile (filled circles) because the column density is no longer spherically symmetric about Io, with the forward cloud profile having the largest column density and showing a distinct change in its slope compared to the trailing cloud profile. The corresponding model profiles for the D_2 emission brightness are given in Fig. 5a. For both the forward and trailing profiles, the calculated eclipse and calculated east–west profiles are in good agreement with each other inside the Lagrange radius, with a maximum brightness of about 200 kR near the exobase. The calculated east–west profile threads the three emission 4 data points for the forward cloud, but falls well below the emission 4 data points in the trailing cloud. For both the forward and trailing clouds at larger radial distances, the calculated east–west profiles fall well below the areas for both the forward and trailing cloud images. This behavior indicates that there is a large deficiency in the high-speed population for this source flux speed distribution.

Model calculations were therefore performed for the second Maxwell–Boltzmann flux distribution in Fig. 3 with a higher most probable speed of v_m = 2.0 km sec^{-1} (i.e., an exobase temperature of ~3690 K) and with a flux ϕ_0 of 1.8 × 10^8 atoms cm^{-2} sec^{-1} (i.e., a total source of ~0.75 × 10^{26} atoms sec^{-1}) and are shown in Figure 4b and Figure 5b. For the D_2 emission brightness profiles in Figure 5b, the calculated east–west profile now threads the center of the forward cloud image area for a radial distance up to about 70 R_{Io} and the lower trailing cloud image area for a radial distance of about 25 R_{Io} before it falls off too steeply. This improved fit at larger radial distances, however, reduces the D_2 emission brightness at the exobase to about 80 kR in Figure 5b and causes the calculated eclipse profile in Figure 4b to fall below the measured eclipse profile for radial distances inside about 3 R_{Io}. The Maxwell–Boltzmann flux distribution therefore cannot fit both the corona profile near Io and the sodium cloud east–west profiles at large distances from the satellite. A flux distribution that has a broader dispersion with enhanced populations for both the low-speed and high-speed atoms is required. The three modified-sputtering flux distributions in Fig. 3, which have a broader dispersion, are thus

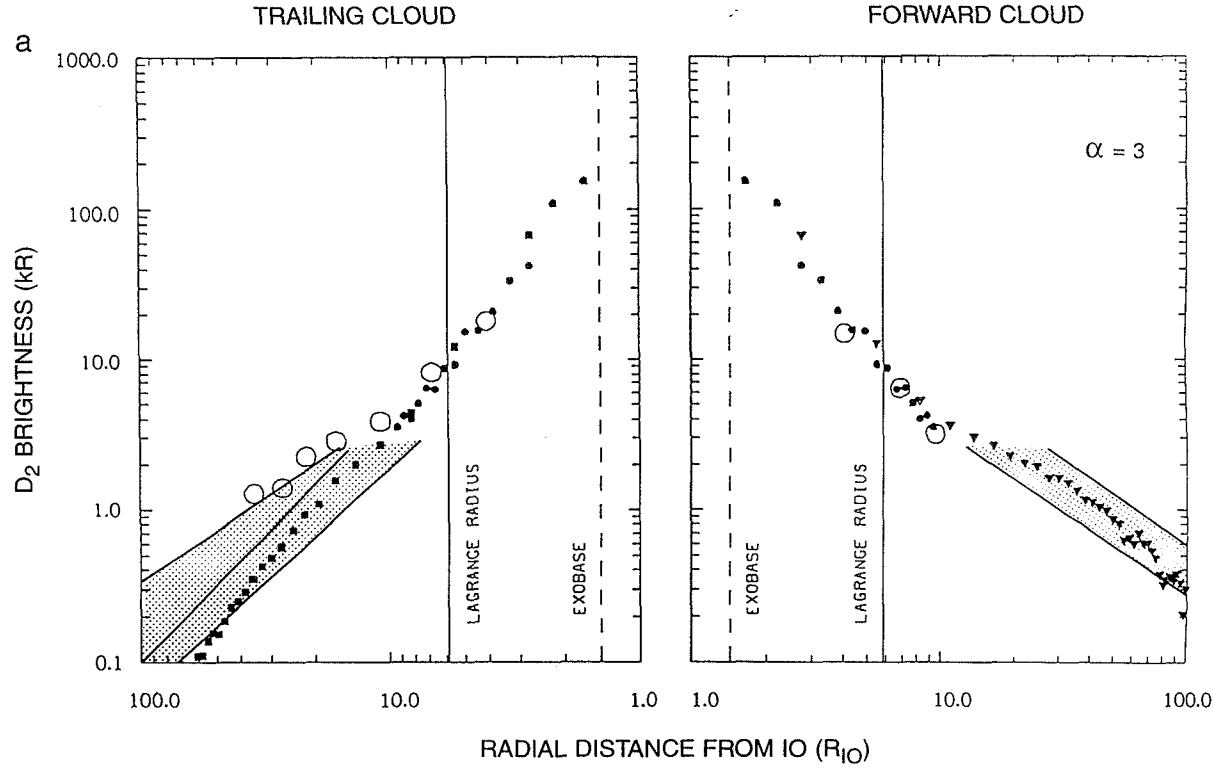

FIG. 7. Model calculations for the east–west D_2 brightness profiles using a modified sputtering flux speed distribution. The east–west D_2 brightness profiles near Io in both the trailing and forward cloud directions determined from the emission 4 data of Schneider *et al.* (1991) are shown by the open circles. The east–west profile envelopes determined from the sodium cloud image data are shown by the shaded areas (see caption of Fig. 2). The descriptions for the calculated profile symbols, the sodium cloud model and plasma torus, and the modified sputtering flux distribution in (a), (b), and (c) are the same as in the caption of Fig. 6.

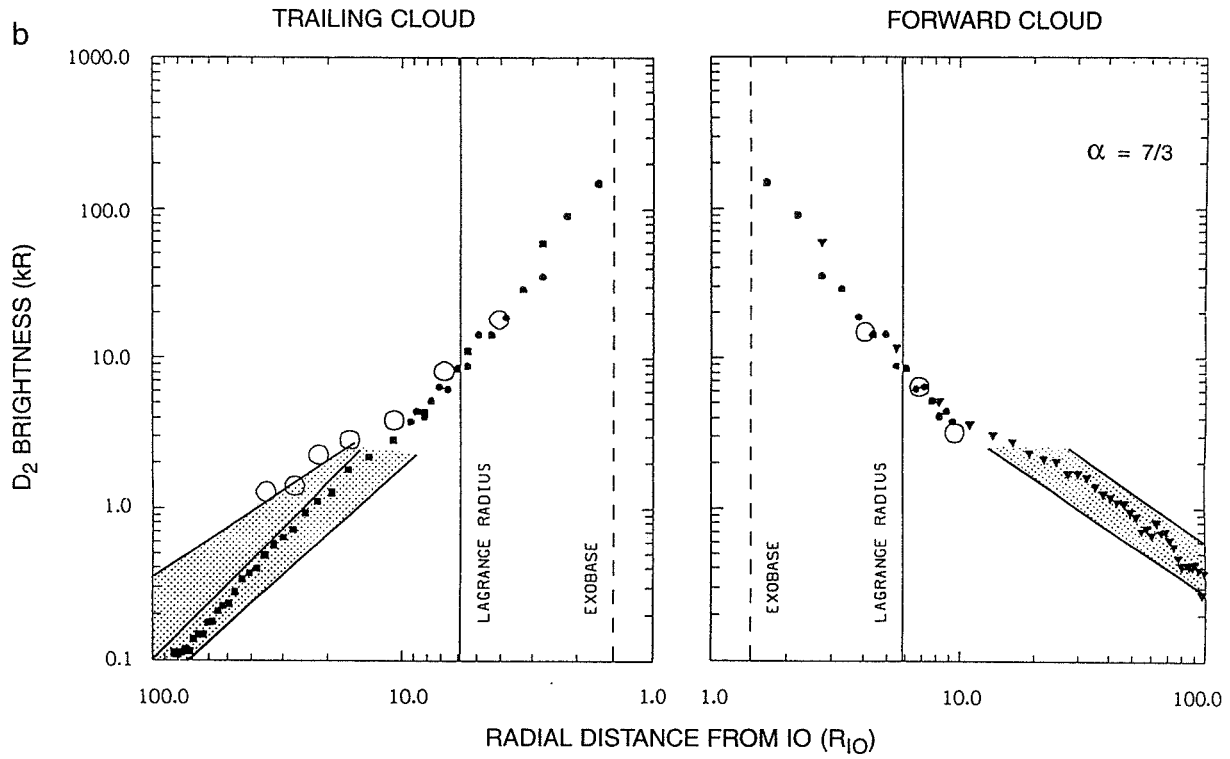

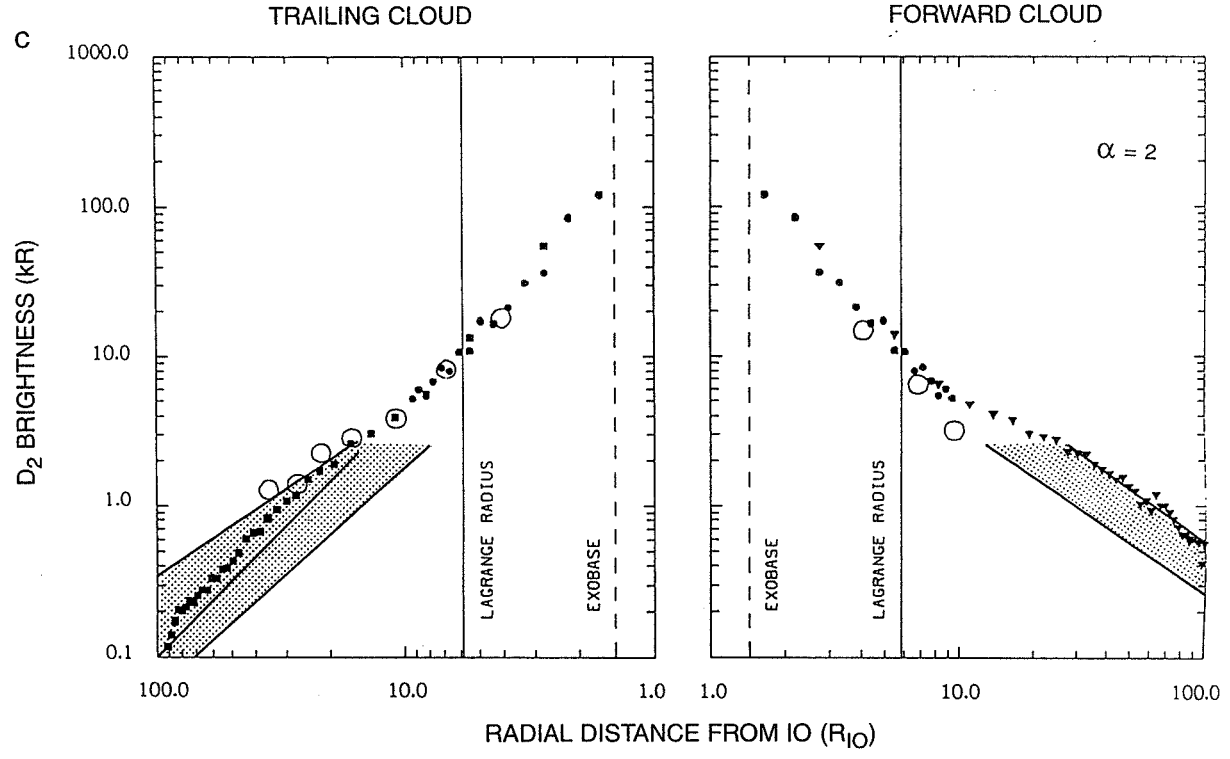

FIGURE 7—*Continued*

TABLE V
Summary Comparison of Modeled and Observed East–West Sodium Profiles for Different Flux Speed Distributions at Io's Exobase

			Corona	Forward Cloud		Trailing Cloud (not null)		Trailing Cloud (null)	
Observations: E/W Radial Interval (R_{Io}):			1.4-6	6-10	10-100	6-10	10-100	6-10	10-100
	Distribution Speed Peak (km/s)	Exobase Source Rate (10^{26} atoms/s)	Fits Eclipse Column Profile	Fits Near Io Emission Profile	Fits Far Cloud E/W Profile	Fits Near Io Emission Profile	Fits Far Cloud E/W Profile	Fits Near Io Emission Profile	Fits Far Cloud E/W Profile
1. Maxwell Boltzmann Flux Distribution									
	1.3	1.24	YES	YES	too low	little low	too low	too low	too low
	2.0	0.75	too low	YES	slightly low	YES	little low	little low	too low
2. Collisional Cascade Flux Distribution									
(classical sputtering)									
$\alpha = 3$	1.0	1.32	YES	YES	tiny low	YES	tiny low	little low	too low
(incomplete cascade: higher velocity tail)									
$\alpha = 7/3$	0.5	1.74	YES	YES	YES	YES	YES	little low	too low
$\alpha = 2$	0.4	1.90	tiny low	too high	too high	too high	too high	YES	YES

considered in the remainder of the paper with model calculations presented in Figs. 6 and 7.

Model calculations for a classical sputtering flux distribution ($\alpha = 3$) and a modified-sputtering flux distribution ($\alpha = 7/3$) are presented in Figs. 6a and 6b for the eclipse observations and in Figs. 7a and 7b for the east–west D_2 emission brightness profiles. For these two flux distributions, the most probable speeds are, respectively, 1.0 km sec^{-1} and 0.5 km sec^{-1}, and the sodium fluxes ϕ_0 are, respectively, 3.2×10^8 atoms cm^{-2} sec^{-1} (i.e., a total source of $\sim 1.3 \times 10^{26}$ atoms sec^{-1}) and 4.2×10^8 atoms cm^{-2} sec^{-1} (i.e., a total source of $\sim 1.7 \times 10^{26}$ atoms sec^{-1}). From the exobase to radial distances of ~ 8 R_{Io}, just beyond the Lagrange radius, both sputtering flux distributions provide a very good fit in Figs. 6a and 6b to the observed eclipse column density profile (open circles) and correspond to an exobase D_2 emission brightness of about 150 kR in Figs. 7a and 7b. For the classical sputtering flux distribution in Fig. 7a, the calculated D_2 emission brightness profile for the forward profile is slightly above the measured data point (open circles) inside the Lagrange radius, matches the two measured data points beyond the Lagrange radius, and then threads the forward cloud image area nicely between about 20 R_{Io} and 80 R_{Io} before it falls too rapidly and drops below this area. An excellent fit for the forward profile is, however, provided by the modified sputtering distribution ($\alpha = 7/3$) in Fig. 7b where the calculated D_2 emission brightness profile matches the measured data points (open circles) both inside and beyond the Lagrange radius as well as nicely threading the forward cloud image area all the way to 100 R_{Io}. For the trailing cloud, the calculated D_2 emission brightness profile for the classical sputtering flux distribution in Fig. 7a matches the measured data point inside the Lagrange radius, is slightly below the two measured data points outside the Lagrange radius, and then threads the lower of the two trailing cloud image areas nicely between about 15 R_{Io} and 35 R_{Io} before it falls too rapidly and drops below this area. An excellent fit for the trailing profile is, however, provided by the modified sputtering distribution ($\alpha = 7/3$) in Fig. 7b where the calculated D_2 emission brightness matches the measured data point inside the Lagrange radius, is slightly below the two measured data points outside the Lagrange radius, and then threads the lower (non-null) trailing cloud image area nicely all the way to 100 R_{Io}. It is particularly noteworthy that the isotropic ejection of sodium from the exobase with a modified sputtering flux distribution with $\alpha = 7/3$ provides a complete fit to the combined eclipse, emission, and forward/trailing sodium cloud image profile data for this non-null condition from 1.4 to 100 R_{Io}.

In order to fit the trailing cloud (upper area) profile for the directional feature at the null condition, it is then clear that a flux distribution is required with an even more enhanced higher-speed population (~ 20 km sec^{-1}) than the modified sputtering flux distribution with $\alpha = 7/3$. Since the modified sputtering flux distribution for $\alpha = 7/3$ corre-

sponds to the limit of a single collision cascade process described by a Thomas–Fermi cross section (see Smyth and Combi 1988b), reducing the value of α to a smaller value becomes somewhat physically questionable but will be used here for the purposes of simply illustrating the impact of a more enhanced higher-speed sodium population in the model calculation. As discussed earlier, this higher-speed sodium is thought to be nonisotropically ejected from Io's exobase and attributed to some combination of direct collisional and lower-velocity charge exchange ejection. Choosing the modified sputtering flux distribution with $\alpha = 2$ in Fig. 3 which has a most probable speed of 0.4 km sec^{-1} and selecting an isotropic exobase source rate of 1.9×10^{26} atoms sec^{-1} (i.e., a flux ϕ_0 of 4.7×10^8 atoms cm^{-2} sec^{-1}), the model-data comparison is shown in Fig. 6c for the eclipse column density and in Fig. 7c for the east–west D_2 emission brightness. The sputtering flux distribution provides a reasonably good fit to the observed column density data points in Fig. 6c with only a small departure very near the exobase and produces a column density profile beyond 10 R_{Io} that is significantly enhanced compared to the $\alpha = 7/3$ case in Fig. 6b. In Fig. 7c, this enhancement in the forward cloud is obvious, where the calculated D_2 emission brightness profile is significantly above the measured data points both inside and outside the Lagrange radius and is above or in the very top of the forward cloud image area all the way to 100 R_{Io}. The additional enhanced high-speed population of the $\alpha = 2$ modified sputtering flux distribution is too large and therefore not consistent with the observed forward profile. In contrast for the trailing cloud in Fig. 7c, the calculated D_2 emission brightness profile matches the measured data points inside and outside of the Lagrange radius very well and then threads the upper of the two trailing cloud image areas nicely all the way to ~90 R_{Io}. This demonstrates that the trailing cloud can be fitted with an enhanced higher-speed population of sodium atoms in the flux distribution. It also immediately demonstrates that the flux distribution at the exobase must be nonisotropic with the enhanced high-speed population weighted toward vector directions that will preferentially populate the trailing cloud. As discussed in Section 2, this nonisotropic requirement for a flux distribution for speeds of ~20 km sec^{-1} is similar to the conclusions reached by earlier modeling analyses (Pilcher *et al.* 1984; Smyth and Combi 1991; Wilson and Schneider 1995).

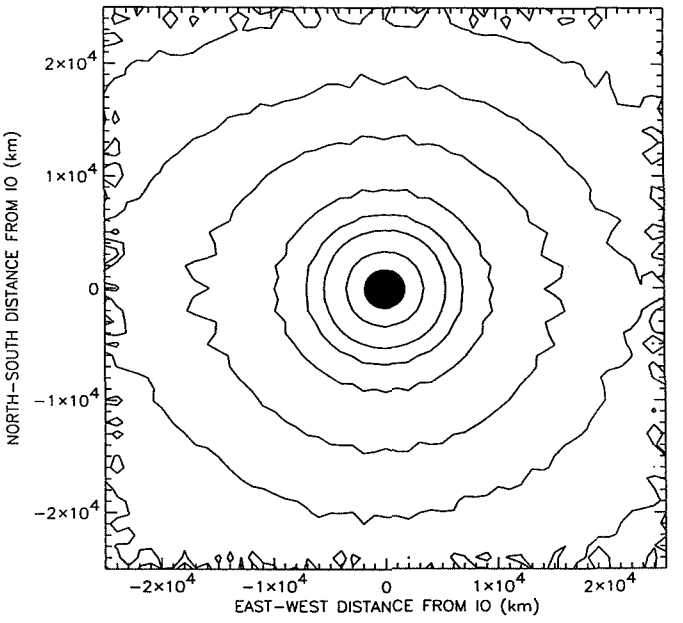

FIG. 8. Two-dimensional nature of the sodium column density near Io. Contours for the two-dimensional column density near Io are shown in the sky-plane of the earth as determined from the sodium cloud model calculation for the modified sputtering flux speed distribution described in Fig. 6(b) for $\alpha = 7/3$. The vertical and horizontal directions are the projected directions that are, respectively, perpendicular and parallel to the semimajor axis of the Io's orbital ellipse on the sky plane. Io's location and size are shown to scale by the black circle. The sodium column density contours in units of 10^{11} atoms cm^{-2} are, from inside to outside, 5, 2, 1, 0.5, 0.2, 0.1, and 0.05.

5. DISCUSSION AND CONCLUSIONS

The composite spatial information for sodium obtained by combining the eclipse observations (radial distances from Io of 1.4 to ~10 R_{Io}), the emission observations (east–west distances of ±4 to ±30–40 R_{Io}), and the sodium cloud observations (east–west distances of ±10 to ±100 R_{Io}) has been analyzed to extract a basic description for the flux speed distribution at the satellite's exobase. An isotropic modified-sputtering flux speed distribution in Fig. 3 with $\alpha = 7/3$, a most probable speed of 0.5 km sec^{-1}, and a source strength of 1.7×10^{26} atoms sec^{-1} provides a very good fit to these composite observations when the directional feature is either north or south and hence not contributing to the east–west profile of the trailing cloud. It is remarkable that these observations, acquired by a number of ground-based programs over very different spatial scales and at different times during the 1976–1985 decade, are so self-consistent. Near Io, the two-dimensional sodium column density produced by this modified sputtering distribution as calculated by the sodium cloud model in the profile analysis above is shown in Fig. 8 and can be seen at larger distances from Io to become nonspherical and more confined near the satellite plane. This flattening near the satellite plane is the merging of the near Io corona into the sodium cloud and is caused naturally by orbital dynamics beyond the satellite Lagrange sphere where the gravity of Jupiter is dominant. The forward cloud portion of the east–west emission data profiles has a rather tightly confined slope that, in the absence of the trailing cloud

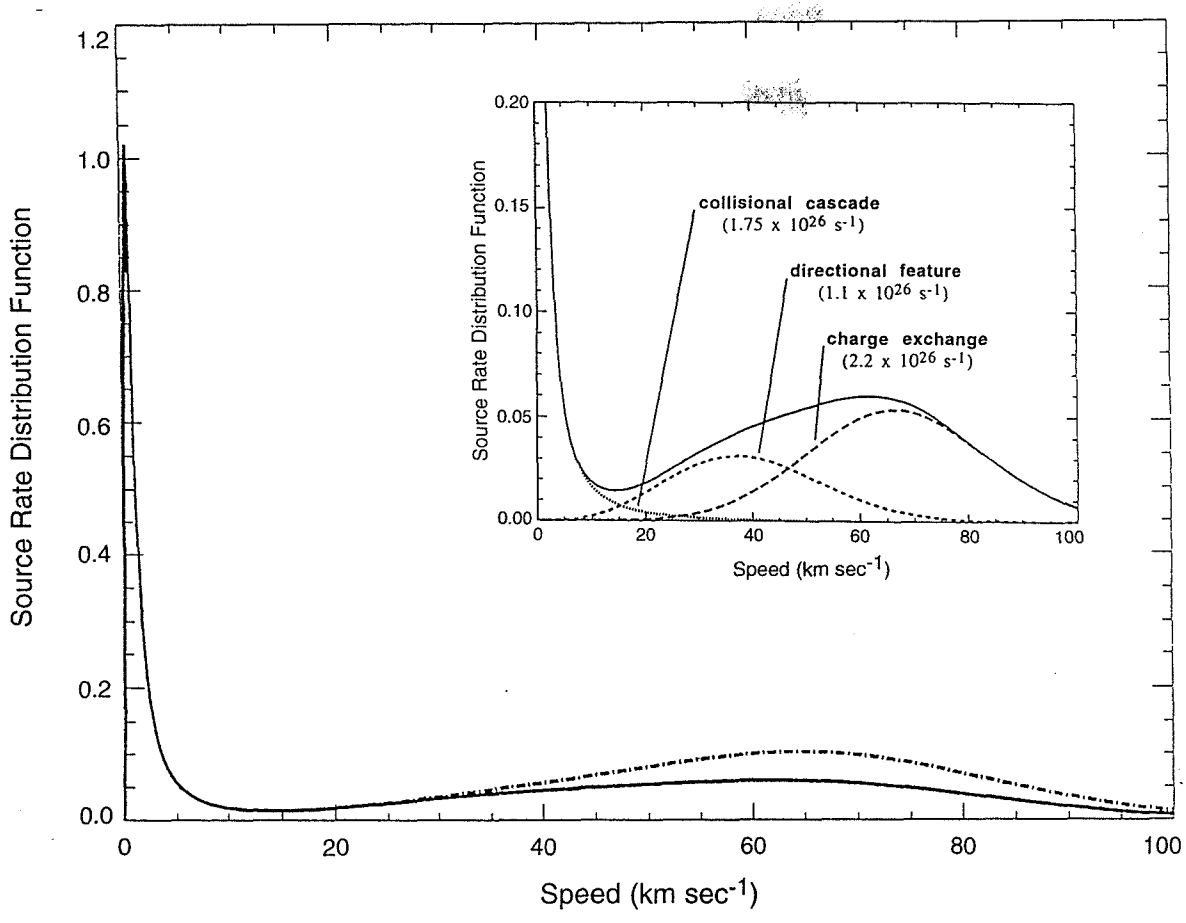

FIG. 9. Total source rate speed distribution function for sodium at Io's exobase. The total source rate speed distribution function at Io's exobase, in units of 10^{26} atoms sec^{-1} $(km/sec)^{-1}$, is composed of three separate source rate speed distributions as discussed in the text and is shown for two different source strengths for the higher-speed zenocorona source centered about 57 km sec^{-1}. The lower (solid line) and upper (dashed-dot line) curves correspond, respectively, to the sodium zenocorona higher-speed source rates of 2.2×10^{26} atoms sec^{-1} (Smyth and Combi 1991) and 4×10^{26} atoms sec^{-1}. The two source rates for the higher-speed zenocorona source are shown to exhibit its typical time-variable source strength range of ~ 2–4×10^{26} atoms sec^{-1} as reported by Flynn *et al.* (1994). The decomposition of the solid curve into its three separate source rate speed distributions is shown in the cutout and is determined by combining (1) the isotropic modified sputtering source rate distribution (dotted line in the cutout) for $\alpha = 7/3$, $v_m = 0.5$ km sec^{-1} and a source strength of 1.7×10^{26} atom sec^{-1}, (2) the nonisotropic lower-speed source rate distribution (short dashed line in the cutout) for the sodium zenocorona and directional feature centered about 20 km sec^{-1}, with a source strength of 1.1×10^{26} atoms sec^{-1} as determined by Smyth and Combi (1991), and (3) the nonisotropic higher-speed source rate distribution (longer dashed line in the cutout) for the sodium zenocorona centered about 57 km sec^{-1}, with a charge exchange source strength of 2.2×10^{26} atoms sec^{-1} as determined by Smyth and Combi (1991).

enhancement at the null condition, is less steep and is brighter than the trailing cloud profiles. In order, however, to reproduce the extended east–west profile in the trailing sodium cloud when the directional feature is in the satellite plane (i.e., the null location), additional nonisotropic high-speed sodium is required.

The sodium atoms ejected from Io's exobase as described above by the modified sputtering flux distribution have speeds primarily in the range from 0 to a few tens of km sec^{-1}. This neutral flux distribution represents the spatially integrated effect of the incomplete collisional cascade process that occurs from the collisional interactions of heavy ions in the corotating plasma torus with neutrals in Io's atmosphere. This flux speed distribution can be alternatively described as a source rate speed distribution by multiplying it by the satellite surface area. In addition to these ion-neutral elastic collisional encounters, resonance charge exchange between plasma torus sodium ions and neutral sodium in Io's atmosphere is also responsible for producing a sodium source with higher speeds relative to Io. These speeds are centered about the corotational ion speed (~ 57 km sec^{-1}) relative to Io's motion and have a dispersion reaching from several tens of km sec^{-1} to ~ 100 km sec^{-1}. Such high speed sodium (≤ 80 km sec^{-1}) has

recently been observed near Io by Cremonese *et al.* (1992). As discussed in Section 2, this higher-speed nonisotropic source of sodium together with the lower speed (~15–20 km sec^{-1}) nonisotropic source for the directional feature form the source for the sodium zenocorona or magneto-nebula. Earlier modeling studies (Smyth and Combi 1991; Flynn *et al.* 1992) indicated that the higher-speed source was $\sim 2 \times 10^{26}$ atoms sec^{-1} while the lower speed source was $\sim 1 \times 10^{26}$ atoms sec^{-1}. More recent observations and analysis (Flynn *et al.* 1994) have shown that the higher-speed sodium source is time variable and in the range ~ 2–4×10^{26} atoms sec^{-1}. A total source rate speed distribution for sodium at Io's exobase has hence been constructed by combining the modified sputtering source rate distribution determined in this paper with the two source rate distribution for the zenocorona as given by Smyth and Combi (1991) and is shown in Fig. 9. The lower (solid line) and upper (dashed-dot line) curves correspond, respectively, to the sodium zenocorona higher-speed source rates of 2.2×10^{26} and 4×10^{26} atoms sec^{-1}. Total source rate speed distribution functions at Io's exobase expected for other atomic species, such as K, O, and S, can be constructed in a similar fashion by adopting the estimated source rates given by Smyth and Combi (1991).

Future studies for the sodium flux speed distribution at Io's exobase are anticipated using much larger data sets now available for east–west and north–south sodium emission observations. It will then be possible to analyze the combined spatial and spectral information and refine the nonisotropic nature of the flux distribution and also to search for other possible east–west and System III related variations. Once this information is determined for sodium, the implications for the more abundant species in Io's atmosphere will be particularly important in other related studies for the many-faceted and complex phenomena in the Io–Jupiter system.

ACKNOWLEDGMENTS

We are grateful to N. M. Schneider for helpful discussions and for providing the numerical data for the 1985 emission observations. We also thank the two referees for their helpful comments. This research was supported by the Planetary Atmospheres Program of the National Aeronautical and Space Administration under Grant NAGW-3585 to the University of Michigan and under Contracts NASW-4416, NASW-4471, and NASW-4804 to Atmospheric and Environmental Research, Inc.

REFERENCES

BERGSTRALH, J. T., D. L. MATSON, AND T. V. JOHNSON 1975. Sodium D-line emission from Io: Synoptic observations from Table Mountain Observatory. *Astrophys. J. Lett.* **195,** L131–L135.

BERGSTRALH, J. T., J. W. YOUNG, D. L. MATSON, AND T. V. JOHNSON 1977. Sodium D-line emission from Io: A second year of synoptic observation from Table Mountain Observatory. *Astrophys. J. Lett.* **211,** L51–L55.

BROWN, R. A. 1974. Optical line emission from Io. In *Exploration of the Planetary System* (A. Woszczyk and C. Iwaniszewska, Eds.), Proceedings IAU Symposium No. 65, Torun, Poland, Sepetember 5–8, 1973, pp. 527–531. Reidel, Dordrecht.

BROWN, R. A., AND Y. L. YUNG 1976. Io, its atmosphere and optical emissions. In *Jupiter: Studies of the Interior, Atmosphere, Magnetosphere, and Satellites* (T. Gehrels, Ed.), pp. 1102–1145. Univ. of Arizona Press, Tucson.

CARLSON, R. W., D. L. MATSON, AND T. V. JOHNSON 1975. Electron impact ionization of Io's sodium emission cloud. *Geophys. Res. Lett.* **2,** 469–472.

CREMONESE, G., N. THOMAS, C. BARBIERI, AND C. PERNECHELE 1992. High resolution spectra of Io's neutral sodium cloud. *Astron. Astrophys.* **256,** 286–298.

FANG, T.-M., W. H. SMYTH, AND M. B. MCELROY 1976. The distribution of long-lived gas clouds emitted by satellites in the outer Solar System, *Planet. Space Sci.* **25,** 577–588.

FLYNN, B. 1993. Oscillating ion streamline model of Jupiter's neutral sodium nebula. *Adv. Space Science* **13,** 325–330.

FLYNN, B., M. MENDILLO, AND J. BAUMGARDNER 1992. Observations and modeling of the jovian remote sodium emission. *Icarus* **99,** 115–130.

FLYNN, B., M. MENDILLO, AND J. BAUMGARDNER 1994. The jovian sodium nebula: Two years of ground-based observations. *J. Geophys. Res.* **99,** 8403–8409.

GOLDBERG, B. A., R. W. CARLSON, D. L. MATSON, AND T. V. JOHNSON 1978. A new asymmetry in Io's sodium cloud, *Bull Am. Astron. Soc.* **10,** 579.

GOLDBERG, B. A., YU. MEKLER, R. W. CARLSON, T. V. JOHNSON, AND D. L. MATSON 1980. Io's sodium emission cloud and the Voyager 1 encounter. *Icarus* **44,** 305–317.

GOLDBERG, B. A., G. W. GARNEAU, AND S. K. LAVOIE 1984. Io's sodium cloud. *Science* **226,** 512–516.

IP, W.-H. 1990. Neutral gas–plasma interaction: The case of the plasma torus, *Adv. Space Res.* **10,** 15–23.

MACY, W. W., JR., AND L. M. TRAFTON 1980. The distribution of sodium in Io's cloud: Implications. *Icarus* **41,** 131–141.

MATSON, D. L., B. A. GOLDBERG, T. V. JOHNSON, AND R. W. CARLSON 1978. Images of Io's sodium cloud. *Science* **199,** 531–533.

MENDILLO, M., J. BAUMGARDNER, B. FLYNN, AND W. J. HUGHES 1990. The extended sodium nebula of Jupiter. *Nature* **348,** 312–314.

MCGRATH, M. A. 1988. *Ion Bombardment of Io and Mercury.* Ph.D. Thesis, Dept. of Astronomy, University of Virginia.

MURCRAY, F. J. 1978. *Observations of Io's Sodium Cloud.* Ph. D. Thesis, Dept. of Physics, Harvard University.

MURCRAY, F. J., AND R. M. GOODY 1978. Pictures of the Io sodium cloud. *Astrophys. J.* **226,** 327–335.

PILCHER, C. B., W. H. SMYTH, M. R. COMBI, AND J. H. FERTEL 1984. Io's sodium directional features: Evidence for a magnetospheric-wind-driven gas escape mechanism. *Astrophys. J.* **287,** 427–444.

SCHNEIDER, N. M. 1988. *Sodium in Io's Extended Atmosphere.* Ph.D. Thesis, Department of Planetary Sciences, Univ. of Arizona.

SCHNEIDER, N. M., D. M. HUNTEN, W. K. WELLS, AND L. M. TRAFTON 1987. Eclipse measurements of Io's sodium atmosphere. *Science,* **238,** 55–58.

SCHNEIDER, N. M., D. M. HUNTEN, W. K. WELLS, A. B. SCHULTZ, AND U. FINK 1991. The structure of Io's corona. *Astrophys. J.* **368,** 298–315.

SIEVEKA, E. M., AND R. E. JOHNSON 1984. Ejection of atoms and molecules from Io by plasma-ion impact, *Astrophys. J.* **287,** 418–426.

SMYTH, W. H. 1979. Io's sodium cloud: Explanation of the east–west asymmetries. *Astrophys. J.* **234,** 1148–1153.

SMYTH, W. H. 1983. Io's sodium cloud: Explanation of the east–west asymmetries. II. *Astrophys. J.* **264,** 708–725.

SMYTH, W. H., AND M. R. COMBI 1987a. Correlating east–west asymmetries in the jovian magnetosphere and the Io sodium cloud, *Geophys. Res. Lett.* **14,** 973–976.

SMYTH, W. H., AND M. R. COMBI 1987b. Time variability of the sodium cloud, poster paper at the international conference "Time-Variable Phenomena in the Jovian System," Flagstaff, Arizona, August 25–27.

SMYTH, W. H., AND M. R. COMBI 1987c. Nature of Io's atmosphere and its interaction with the planetary magnetosphere. *Bull. Am. Astron. Soc.* **19,** 855.

SMYTH, W. H., AND M. R. COMBI 1988a. A general model for Io's neutral gas cloud. I. Mathematical description. *Astrophys. J. Supp.* **66,** 397–411.

SMYTH, W. H., AND M. R. COMBI 1988b. A general model for Io's neutral gas clouds. II. Application to the sodium cloud. *Astrophys. J.* **328,** 888–918.

SMYTH, W. H., AND M. R. COMBI 1991. The sodium zenocorona. *J. Geophys. Res.* **96,** 22711–22727.

SMYTH, W. H., AND B. A. GOLDBERG 1993. The Io sodium cloud: Space–time signatures of east–west and system III longitudinal asymmetries in the jovian magnetosphere. Paper presented at Io: An international conference, San Juan Capistrano, California, June 22–25.

SMYTH, W. H., AND M. B. MCELROY 1977. The sodium and hydrogen gas clouds of Io, *Planet. Space Sci.* **25,** 415–431.

SMYTH, W. H., AND M. B. MCELROY 1978. Io's sodium cloud: Comparison of models and two-dimensional images. *Astrophys. J.* **226,** 336–346.

SUMMERS, M. E., D. F. STROBEL, Y. L. YUNG, J. T. TRAUGER, AND F. MILLS 1989. The structure of Io's thermal corona and implications for atmospheric escape. *Astrophys. J.* **343,** 468–480.

TRAFTON, L., AND W. MACY, JR. 1978. On the distribution of sodium in the vicinity of Io, *Icarus* **33,** 322–335.

WILSON, J. K., AND N. M. SCHNEIDER 1994. Io's fast sodium: Implications for molecular and atomic atmospheric escape, *Icarus* **111,** 31–44.

WILSON, J. K., AND N. M. SCHNEIDER 1995. Io's sodium directional feature: Evidence for ionospheric rip-off, *Bull. Am. Astron. Soc.* **27,** 1154.

REPORT DOCUMENTATION PAGE

Form Approved
OMB No. 0704-0188

1. AGENCY USE ONLY (Leave blank)	2. REPORT DATE	3. REPORT TYPE AND DATES COVERED
	June 19, 1997	Bi-Monthly March 22-May 22, 1997

4. TITLE AND SUBTITLE
Studies for the Loss of Atomic and Molecular Species from Io

5. FUNDING NUMBERS

6. AUTHOR(S)
William H. Smyth

7. PERFORMING ORGANIZATION NAME(S) AND ADDRESS(ES)
Atmospheric and Environmental Research, Inc.
840 Memorial Drive
Cambridge, MA 02139

8. PERFORMING ORGANIZATION REPORT NUMBER
P-658

9. SPONSORING/MONITORING AGENCY NAME(S) AND ADDRESS(ES)
NASA Headquarters
Headquarters Contract Division
Washington, DC 20546

10. SPONSORING/MONITORING AGENCY REPORT NUMBER

11. SUPPLEMENTARY NOTES

12a. DISTRIBUTION/AVAILABILITY STATEMENT

12b. DISTRIBUTION CODE

13. ABSTRACT *(Maximum 200 words)*

For Io neutral cloud calculations, an SO_2 source strength of ~$4x10^{27}$ molecules/sec was determined by successfully matching the SO_2^+ density profile near the satellite deduced from magnetometer data acquired by the Galileo spacecraft during its close flyby on December 7, 1995. The incomplete collision source velocity distribution for SO_2 is the same as recently determined for the trace species atomic sodium by Smyth and Combi (1997). Estimates for the total energy loss rate (i.e. power) of O and S atoms escaping Io were also determined and imply a significant pickup current and a significant reduction in the local planetary magnetic field near Io.

14. SUBJECT TERMS
Io, satellite Atmospheres

15. NUMBER OF PAGES
28

16. PRICE CODE

17. SECURITY CLASSIFICATION OF REPORT	18. SECURITY CLASSIFICATION OF THIS PAGE	19. SECURITY CLASSIFICATION OF ABSTRACT	20. LIMITATION OF ABSTRACT
Unclassified	Unclassified	Unclassified	